RESEARCH ARTICLE

ADVANCED MATERIALS
www.advmat.de

Programmable Surface Dimpling of Textile Metamaterials for Aerodynamic Control

*David T. Farrell, Connor M. McCann, Antonio Elia Forte, Conor J. Walsh, and Katia Bertoldi**

Static aerodynamic surfaces are inherently limited in their ability to adapt to dynamic velocity profiles or environmental changes, restricting their performance under variable operating conditions. This challenge is particularly pronounced in high-speed competitive sports, such as cycling and downhill skiing, where the properties of a static textile surface are mismatched with highly dynamic wind-speed profiles. Here, an textile metamaterial is introduced that is capable of variable aerodynamic profiles through a stretch-induced dimpling mechanism, even when tightly conformed to a body or object. Wind-tunnel experiments are used to characterize the variable aerodynamic performance of the dimpling mechanism, while Finite Element (FE) simulations efficiently characterize the design space to identify optimal textile metamaterial architectures. By controlling dimple size, the aerodynamic performance of the textile can be tailored for specific wind-speed ranges, resulting in an ability to modulate drag force at target wind-speeds by up to 20%. Furthermore, the potential for active control of a textiles' aerodynamic properties is demonstrated, in which controlled stretching allows the textile to sustain optimal performance across a dynamic wind-speed profile. These findings establish a new approach to aerodynamic metamaterials, with surface dimpling and thus variable fluid-dynamic properties offering transformative applications for wearables, as well as broader opportunities for aerospace, maritime, and civil engineering systems.

1. Introduction

In high-speed sports, marginal differences in air resistance can have a compounding impact over time, making aerodynamics a critical factor for determining competitive success.[1–4] Depending on the interplay between the athlete's posture and the surface properties of the garments they wear, pressure drag is generated by a low-pressure zone localized behind the body, which in turn produces air resistance.[5,6] At a critical Reynolds number, this low-pressure zone collapses due to an aerodynamic instability known as drag crisis,[7] resulting in a substantial reduction in drag. However, at lower Reynolds numbers such instabilities do not take place. Within these regimes, a common method to induce early drag crisis is to increase the surface roughness, effectively reducing drag at lower speeds compared to a smooth surface.[8–11] Whilst a classic example of roughness induced drag reduction is the dimples on a golf ball,[12] the concept has also been applied to textiles to reduce aerodynamic drag on the human body.[1,6,13–19] By tailoring textile roughness, researchers have achieved reductions of 40–50% in aerodynamic drag at specific wind speeds.[6,13,17,19,20] However, practical applications span a range of wind speeds, which compromise the efficiency of such designs, therefore a strategy to adapt roughness and optimize drag reduction at dynamic wind speeds is desirable.[5,21,22]

Surfaces with variable roughness can be tuned to maximize performance at multiple velocities. These aerodynamic systems have been previously demonstrated using pneumatic actuation in soft-dimpled elastomeric membranes[23–25] and aerofoils.[26] For wearable applications, small-scale surface adjustments induced by yarn-separation in textiles have been shown to modify aerodynamic properties while maintaining a snug fit on the body.[14,15,27,28] Although these effects are typically limited and primarily occur at high Reynolds numbers,[29] recent research has demonstrated that introducing macro-textile structures, such as knitted grooves, into textiles can significantly enhance aerodynamic adaptability but still require large strains for minimal changes in surface roughness.[30] Wrinkling,[31–34] also present a promising mechanism for generating load-dependent macroscopic roughness. However, in worn textiles, these wrinkles are often suppressed due to the boundary conditions and curvature imposed by the body.[35]

Motivated by these recent advances, we introduce textile metamaterials designed to promote and actively control mesoscale dimples on tight-fitting textiles. Our textile metamaterial consists of a stiff woven fabric bonded to a spandex knit. Guided by FE

D. T. Farrell, C. M. McCann, A. E. Forte, C. J. Walsh, K. Bertoldi
John A. Paulson School of Engineering and Applied Sciences
Harvard University
Cambridge, MA 02138, USA
E-mail: bertoldi@seas.harvard.edu

A. E. Forte
Department of Engineering
King's College London
London WC2R 2LS, UK

The ORCID identification number(s) for the author(s) of this article can be found under https://doi.org/10.1002/adma.202505817

DOI: 10.1002/adma.202505817

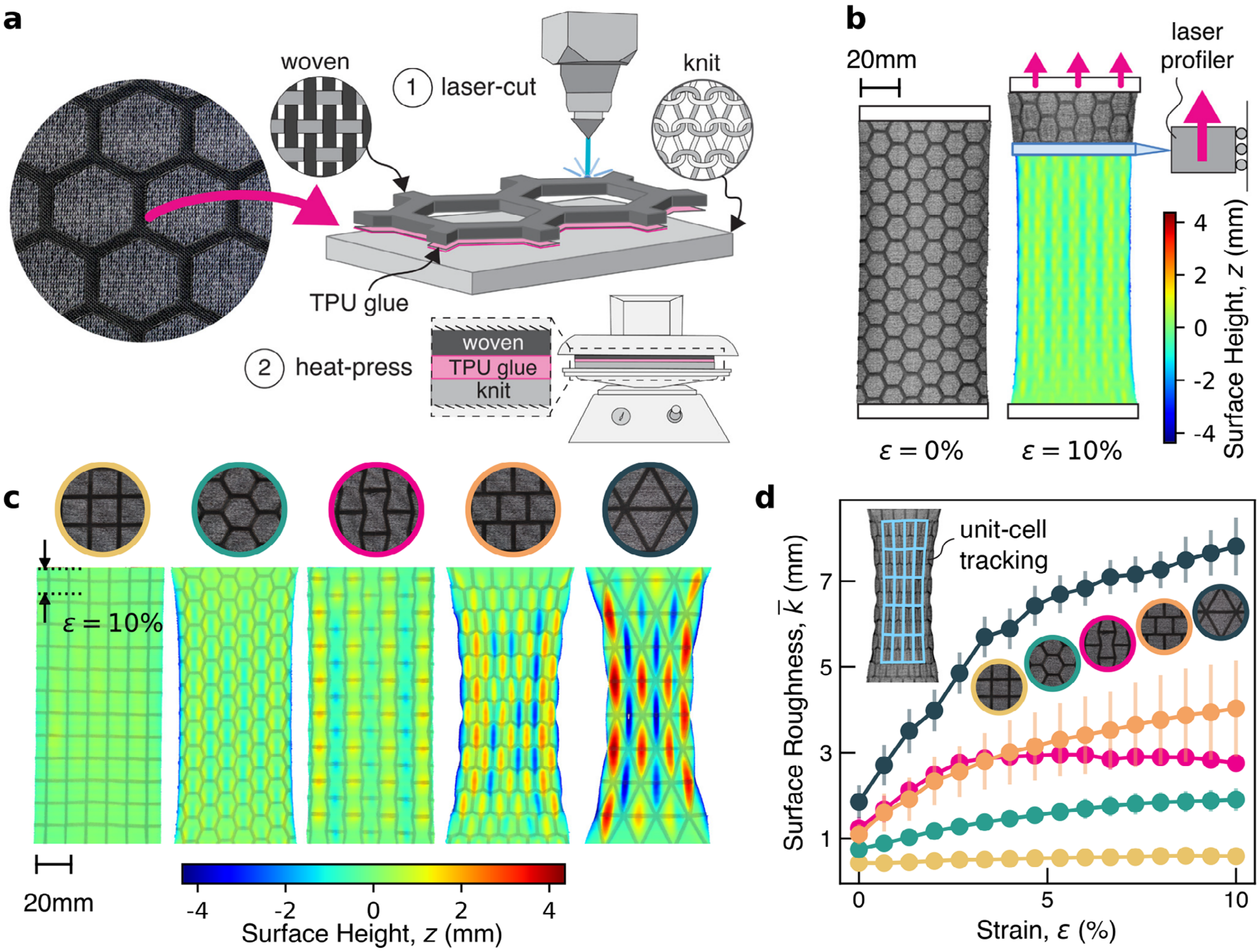

Figure 1. Textile Metamaterials. a) A textile metamaterial is created by laminating a soft knit and a patterned woven fabric using a thermally activated adhesive. b) Snapshots of a planar textile metamaterial sample with a hexagonal pattern in its undeformed (left) and stretched (right) states. The experimentally measured surface profile is overlaid on the stretched sample. c) Snapshots of all investigated planar textile metamaterials in the stretched configuration, with the experimentally measured surface profile overlaid. d) Evolution of surface roughness as a function of applied strain for all tested planar samples, with roughness depicted as average of experimental data (dots) and standard deviation (shaded bars).

simulations, we demonstrate that by varying the architecture of the woven fabric, we can significantly alter the shape, location, and surface roughness of the dimples on the worn textile, as well as their evolution under applied deformation. Notably, by tuning dimple magnitude, we can selectively modulate the drag of a textile-wrapped cylindrical shape, as measured in a wind-tunnel setting. More importantly, we show that by controlling the applied deformation, we can actively tune the dimples to maintain minimal drag force under varying wind speeds. These advancements open the door to a new generation of adaptable, aerodynamic textiles.

2. Results

2.1. Textile Metamaterials

Taking inspiration from the field of flexible mechanical metamaterials,[36–38] we have developed a textile metamaterial platform to promote and actively control mesoscale dimples on worn textiles. Our approach combines the stiffness of a woven textile with the soft-compliance of a spandex knit, creating a textile metamaterial with tunable material properties. Using a two-step manufacturing process, we laser-cut periodic patterns into the woven fabric, which is then heat-pressed together with the knit layer using a pre-applied thermal adhesive to form a textile composite (**Figure** 1a; Video S1 and Supporting Information for additional details). This straightforward, two step manufacturing process also enables rapid design iteration, with each batch of samples requiring 30–60 minutes to manufacture using accessible, non-specialized equipment. With an approximate composite thickness of 0.65 mm, the textile metamaterial remains comfortable and conforms easily to the body.

Initially to explore the capabilities of the textile metamaterial, we fabricated flat samples patterned into five common periodic lattices: square, hexagonal, re-entrant, offset square, and triangular. These designs, widely studied in metamaterial literature,[39,40] enabled a systematic exploration of how tessellations affect the mechanical response of the resulting textile metamaterials. The patterns' units consist of connected woven ligaments | e.g., the square is composed by four straight ligaments connected end-to-end to form a close loop. In all patterns the woven ligaments are cut with a width of 2.25 mm, and the length of the ligaments is chosen to achieve a woven area fraction of ≈33%. We then stretch these sample uniaxially by applying a uniaxial strain, ε, and scan the surface profile using a high-resolution laser profiler (Keyence LJ-X8200), which provides surface profiles accurate to within ±27 μm (Figure 1b). By stretching and scanning in 1 mm increments up to 10% strain, we captured detailed changes in surface roughness over a feasible range of on-body actuation strains.

The woven layer, being approximately 300 times stiffer than the underlying knit, imposes significant constraints on the deformation of the knit during loading, leading to mechanical frustration. In most patterns (except for the square one) this results in the formation of dimples with an area comparable to the size of a unit cell (see Figure 1c). The dimples exhibit oblong, dome-like shapes, with surface heights varying based on the unit-cell pattern. Unlike traditional membrane wrinkling, which typically emerges as a deformation field with localized necking,[32–35] the dimples observed here are distributed across the entire sample, including unit cells near the clamped boundaries. At $\varepsilon = 10\%$, dimple surface heights range from 1 mm in the hexagonal lattice to 4 mm in the triangular lattice. The surface heights of the dimples correlates with the degree of lateral contraction in the samples, with the triangular pattern exhibiting the highest lateral contraction. Additionally, the dimple orientation – whether they form inward or outward – is influenced by the structural imperfections in the textile. However, the dimples are bistable and can be manually inverted through localized deformation.

The mean change in surface roughness due to dimpling can be quantified as

$$\bar{k} = \frac{1}{N}\sum_{i=1}^{N}(z_{\max,i} - z_{\min,i}) \tag{1}$$

where $z_{\min,\,i}$ and $z_{\max,\,i}$ denote the minimum and maximum out-of-plane displacement for the i-th unit cell and N is the number of unit cells. Unit cells are segmented (inset in Figure 1d) and tracked using the Lucas-Kanade optical flow method (further details available in Supplemental Method S2.1.1). As shown in Figure 1d, the evolution of $\bar{k}$ as a function of ε is strongly influenced by the woven pattern, exhibiting a nonlinear relationship that tends to plateau as ε approaches 10%. As expected, the triangular woven lattice produces the largest $\bar{k}$ across the examined range of ε, while the surface roughness of the square woven lattice remains largely unaffected by the applied deformation. Finally, it is important to note that all samples exhibit an initial non-zero $\bar{k}$ at zero strain due to the inherent surface roughness and localized slack within the textile structure.

2.2. On-Body Boundary Conditions

Next, to assess the on-body performance of the textile metamaterials under skin-tight conditions, we wrap textile metamaterial sleeves around an acrylic cylinder with a diameter of $D = 57.15$ mm (**Figure 2a**). During testing, we axially stretch the metamaterial sleeve and rotate the cylinder using a custom setup to scan the metamaterial surface with a laser profiler (Figure 2b - see Supporting Information S2.2.1 for experimental details).

Interestingly, under these boundary conditions, at $\varepsilon = 10\%$ all samples fail to form pronounced dimples, except for the re-entrant pattern (Figure 2c), which exhibits domed dimples protruding from the surface of the cylinder (Figure 2d). Figure 2e reports the evolution of $\bar{k}$ with respect to applied strain. To account for curvature, the dimensionless parameter $\bar{k}/D$ is introduced and is shown in Figure 2e. Similar to the planar case, all samples exhibit non-zero roughness at $\varepsilon = 0\%$ due to the inherent textile roughness. However, as strain increases, the hexagonal, offset-square, and triangular designs exhibit minimal dimpling due to boundary constraints. For instance, the change in roughness of the triangular sample at $\varepsilon = 10\%$ is 30 times smaller than in the planar case. In contrast, the re-entrant design buckles and forms dimples immediately, displaying a similar plateau in the roughness-strain relationship to the planar case. This distinct behavior observed in the re-entrant sample wrapped around the cylinder can be attributed to the Poisson's ratio of the textile metamaterials. All designs, except for the re-entrant design, exhibit a positive Poisson's ratio (see Supporting Information for details S3.2.3). Typically, for a cylindrical membrane subjected to axial strain, a positive Poisson's ratio would result in a reduction in both radius and circumference. However, these dimensions are now constrained by the underlying acrylic tube. As a result, these positive Poisson's ratio textile metamaterial becomes tighter and contact forces inhibit the formation of dimples. In contrast, the re-entrant pattern, characterized by a negative Poisson's ratio, allows for expansion in the circumferential direction, facilitating dimple formation.

2.3. Aerodynamic Testing

Motivated by the distinctive dimpling patterns exhibited by the re-entrant textile worn on cylindrical surfaces, we seek to address a key question: How do these dimples impact aerodynamic performance under varying strain levels? To address this, experiments were conducted using textile-wrapped cylinders in an open-return wind tunnel with the cylinders orientated transversely to the incoming airflow (**Figure 3a**). Although testing on textile-wrapped cylinders does not replicate the full complexity of on-body aerodynamic conditions, a measurable reduction of drag resistance under these simplified conditions still serves as a reliable indicator of potential aerodynamic benefits.[5] Wind speed, U, was measured using a high-precision hot-wire anemometer and open-loop control was used to slowly vary the wind speed from approximately 7.8–26.4 m/s. Further, the drag force acting on the cylinders, F_d, was recorded via a load-cell transducer (see Supporting Information for further details S2.2.2).

Since the projected area of the sample is relatively large compared to the cross-sectional area of the wind tunnel, blockage

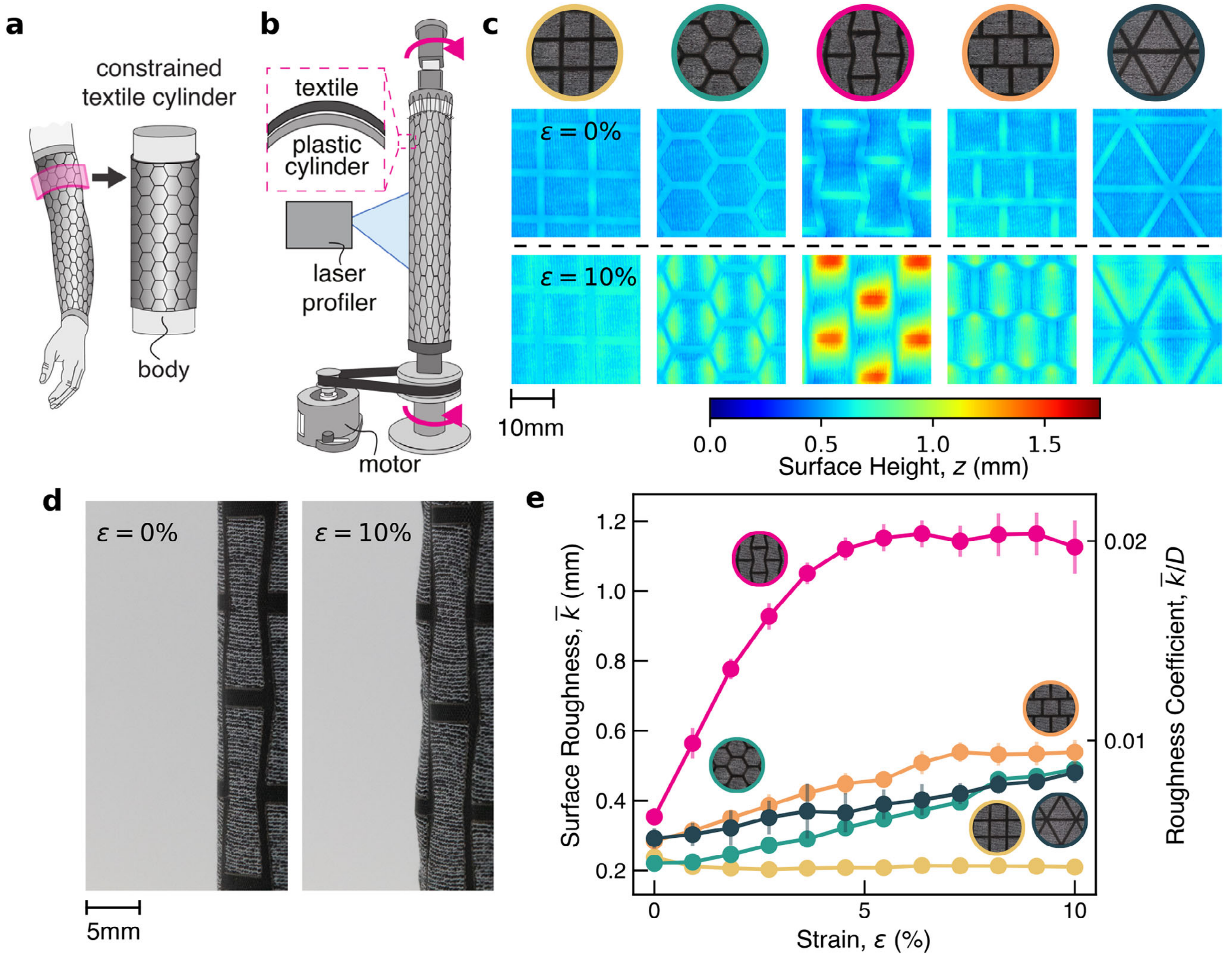

Figure 2. On-body Boundary Conditions. a) To replicate on-body boundary conditions, textile metamaterial sleeves are wrapped around a cylindrical surface. b) Schematic of the setup used for sample characterization. c) Snapshots of the central region of all investigated samples in their undeformed (top) and stretched (bottom) states, with the experimentally measured surface profile overlaid. d) Snapshot of the re-entrant textile metamaterial in its undeformed (left) and stretched (right) states. e) Evolution of surface roughness as a function of applied strain for all tested samples, with roughness depicted as average of experimental data (dots) and standard deviation (shaded bars).

effects, quantified by the blockage ratio $\beta = DL/L^2 = 0.19$ ($L = 305$ mm being the length of the cylinder), must be taken into account.[23,24,41] For this, we applied Maskell's theory[41] to calculate the corrected drag cofficient, C_d, as

$$C_d = \frac{\overline{C}_d}{(1 + \zeta \beta \overline{C}_d)} \tag{2}$$

where $\overline{C}_d$ is the uncorrected drag coefficient

$$\overline{C}_d = \frac{2F_d}{\rho U^2 DL} \tag{3}$$

with ρ denoting the density of air at ambient room temperature conditions. Further, $\zeta = 0.343$ is a numerical constant determined by fitting experimental results for smooth cylinders to well-established predictions[7] (see Supporting Information for additional details S2.2.2).

In Figures 3b,c, we report the evolution of the drag coefficient as a function of the wind speed for cylinders wrapped with knit and re-entrant textile metamaterials, respectively, under varying levels of applied strain. Additionally, a target speed region is overlaid on these graphs to underscore the aerodynamic speeds typically encountered in high-speed sports. We report these speeds with the corresponding Reynolds number, defined as

$$Re = \frac{UD}{\upsilon} \tag{4}$$

where υ is the kinematic viscosity of air at room temperature. The knit sample serves as the baseline for aerodynamic properties, representing a tight-fitting spandex knit. In the undeformed configuration, the drag coefficient of the knit textile aligns with lit-

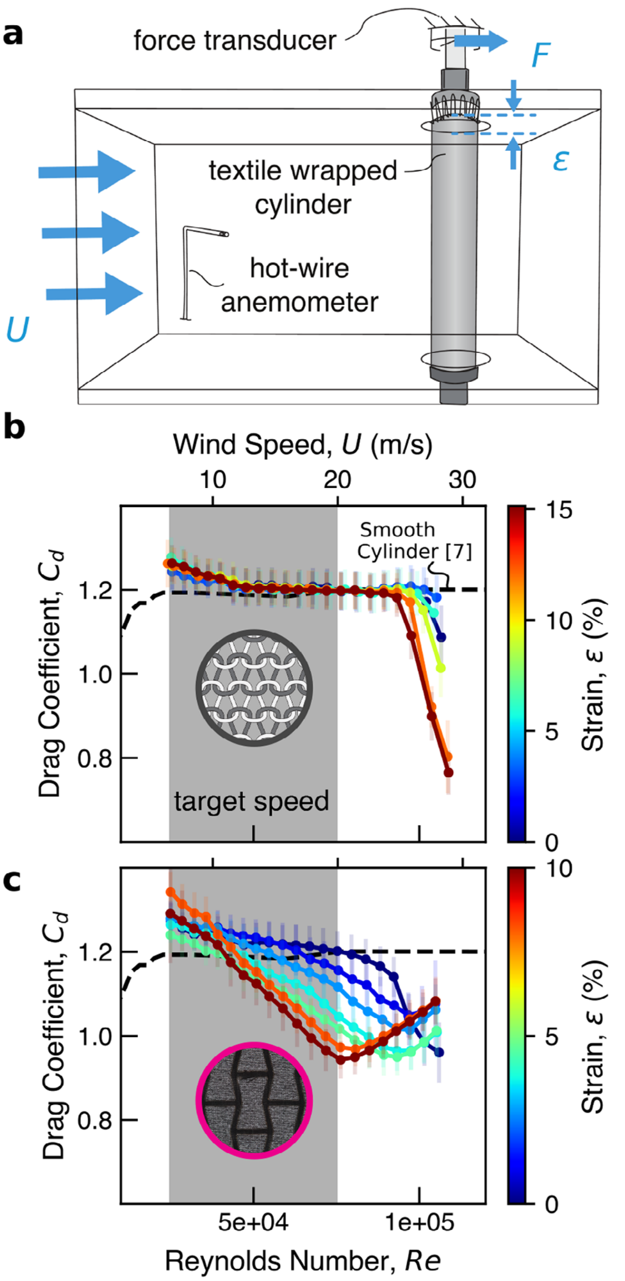

Figure 3. Aerodynamic Testing. a) Schematic of the open-return wind tunnel with a textile-wrapped cylinder inside. b,c) Drag coefficient as a function of Reynolds number for different levels of applied strain in (b) a spandex knit and (c) the re-entrant textile metamaterial from Figure 2. Error bars indicate standard deviation for each averaged time-period. For reference, the curve for a smooth cylinder without the textile sleeve is shown as a dashed black line.

erature values for smooth cylinders ($C_d \approx 1.2$) for approximately $10 < U < 27.5$ m/s.[7] For values of $U < 10$ m/s, the coefficient of drag appears slightly higher, which is attributed to the deviations in blockage corrections. Upon stretching, the individual stitches of the knit separate, slightly increasing surface roughness. This change induces a drop in the drag coefficient at higher wind speeds ($U > 25$ m/s). In contrast, the re-entrant textile metamaterial exhibits significant stretching-induced changes in aerodynamic performance across a wider range of wind speeds (Figure 3c). The formation of dimples caused by stretching substantially increases surface roughness compared to the knit. This enhanced roughness lowers the wind speed at which the drag crisis occurs, resulting in a 20% reduction in drag force compared to the knit sample at 20 m/s and approximately 10% strain. As the re-entrant sample is stretched, the dimple surface roughness plateaus and the aerodynamic change stabilizes, with a minimum drag coefficient of 0.95 near 20 m/s.

2.4. Programming Dimples in Re-entrant Textile Metamaterials

To achieve greater control over the aerodynamic properties of textile metamaterials, we systematically explored the design space of the re-entrant lattices, investigating the effects of three geometric parameters: width (w), height (h), and internal angle (α) (**Figure** 4a). For this purpose, we conducted nonlinear FE analyses using Abaqus/Standard. To reduce computational times, we simulated representative volume elements that were meshed using shell elements and subjected to periodic boundary conditions. Additionally, contact interactions with a rigid surface were included and the mechanical response of the knit and woven materials was modeled using a Ogden hyperelastic formulation[42] and the anisotropic linear lamina model,[43] respectively. We simulated the stretching process by running implicit dynamic simulations and monitored the evolution of the surface profile (see Supporting Information S3 for details).

To best understand the impact of changes to the geometric parameters, the simulation of a substantial number of geometries was undertaken. We simulated geometries with $w \in [10, 22]$mm, $h \in [12, 43]$mm and $\alpha \in [38°, 86°]$. In Figure 4b we report the dimple depth k at $\varepsilon = 10\%$ and the re-entrant area $A = w \times h$ for all designs. Two key features are evident from the sampling. First, by comparing the results with those obtained for the design considered in Figure 2 (indicated by magenta markers and labeled as G1 in Figure 4b), we find that appropriately tuning the geometry can significantly influence the dimple depth. As expected, larger unit cells can achieve greater dimple depths, but only if the geometry of the re-entrant unit is properly tuned. Second, while all dimples initially formed in the center of the horizontal ligaments, for 64% of the designs tested, these centered dimples eventually collapsed into two smaller dimples near the ends of the horizontal ligaments. Importantly this splitting process leads to dimples with smaller depth (see gray markers in Figure 4b - see Supporting Information S3.4).

Based on these results, we selected three geometries that exhibit the largest k values for three distinct unit-cell areas, denoted as G2, G3, and G4 in Figure 4b. The parameters defining these designs are (w, h, α)=(10 mm, 20 mm, 73.3 °), (14 mm, 22 mm, 66.0°) and (15 mm, 30 mm, 70.7°) for G2, G3, and G4, respectively. In Figure 4c we present the evolution of the surface roughness k as a function of the applied strain for these three designs. Note that to compare experimental data with simulated deformation, the experimental surface roughness measurements were adjusted by subtracting the initial surface roughness of the knit-woven microstructure prior to stretching, k_0. Similar to the initial re-entrant design (G1, represented by the magenta dashed line), k

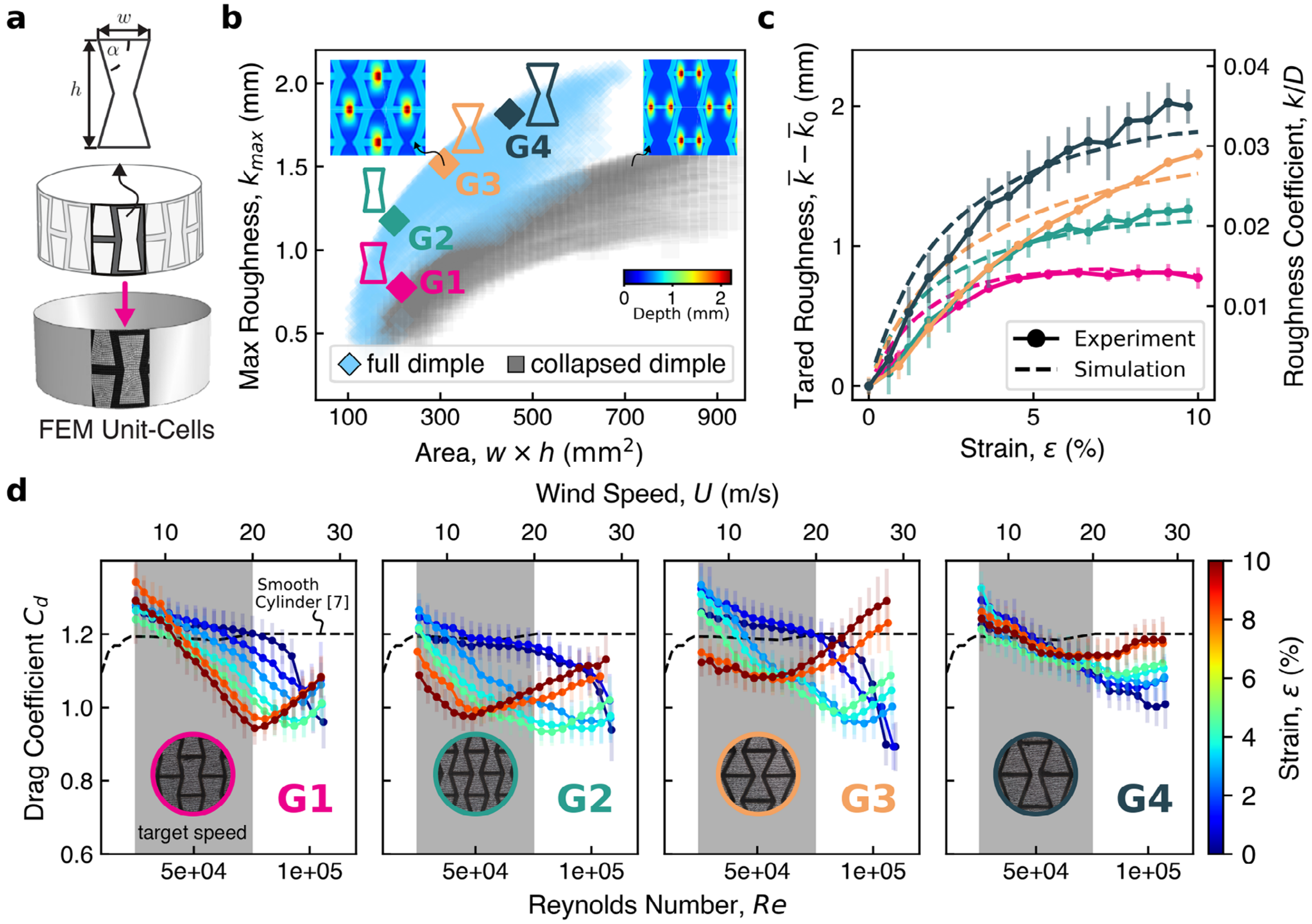

Figure 4. Programming Dimples in Re-entrant Textile Metamaterials. a) Schematic of the parameterized re-entrant textile metamaterial. b) Maximum surface roughness at 10% strain (k_{max}) as a function of re-entrant area (A) for all simulated re-entrant textile metamaterials. c) Evolution of surface roughness with applied strain for geometries G1–G4, with roughness depicted as average of experimental data (dots) and standard deviation (shaded bars). d) Drag coefficient as a function of Reynolds number for different levels of applied strain in geometries G1–G4. Error bars indicate standard deviation for each averaged time-period.

for sample G2, G3, and G4 increases sharply at first but gradually levels off. However, as highlighted in Figure 4b, the plateau value of k varies significantly with geometry, reaching its maximum for G4 close to 2 mm.

Next, we characterized the aerodynamic performance of the three selected designs. The aerodynamic results are presented for all re-entrant designs in Figure 4d, with the initial re-entrant design (G1) included as a baseline for comparison. Prior to stretching (at $\varepsilon = 0$), all samples exhibit similar drag coefficients ($C_d \approx 1.2$). Upon stretching, G2 shows a significant reduction in drag coefficient, reaching a minimum value of 0.93 at $\varepsilon = 4.5\%$. Notably, the critical Reynolds number for G2 occurs at a lower values compared to G1, with substantial drag reductions observed within the target wind speed range of $6.5 < U < 20$ m/s. In contrast, designs G3 and G4, which produce the largest dimples, provide limited aerodynamic benefits. At low levels of strain ($\varepsilon < 3\%$), the dimples of samples G3 and G4 are insufficiently pronounced to meaningfully alter the aerodynamic behavior. However, as the applied strain increases, the dimples become significantly larger, likely shifting the critical Reynolds number below the wind speed range tested in our experiments ($U < 6.5$ m/s). As a result, within the tested wind speed range, the sample operates in the post-critical regime, where the increased surface roughness negatively impacts aerodynamic performance, leading to higher drag coefficients at elevated speeds.[11,44] Together, these results suggest that the dimpling behavior of G2 is best suited to the given cylinder diameter and the target range of low wind speeds. Smaller dimple heights in G1 fail to shift the critical Reynolds number into the target range, while larger dimples in G3 and G4 result in post-critical saturation effects.

2.5. Active Dimpling Control

Expanding on the findings in Figure 4, we exploit the aerodynamic properties of design G2 to achieve active aerodynamic control. As shown in **Figure 5a**, the minimum drag coefficient for design G2 is achieved by applying $\varepsilon = 10\%$ for wind speeds below 15 m/s and $\varepsilon = 5\%$ for wind speeds above 15 m/s. As such, for a wind speed profile representative of high-speed sporting applications spanning $U \in [7.5, 17]$ m/s (Figure 5b), optimal drag resistance can be attained by applying $\varepsilon = 10\%$ during

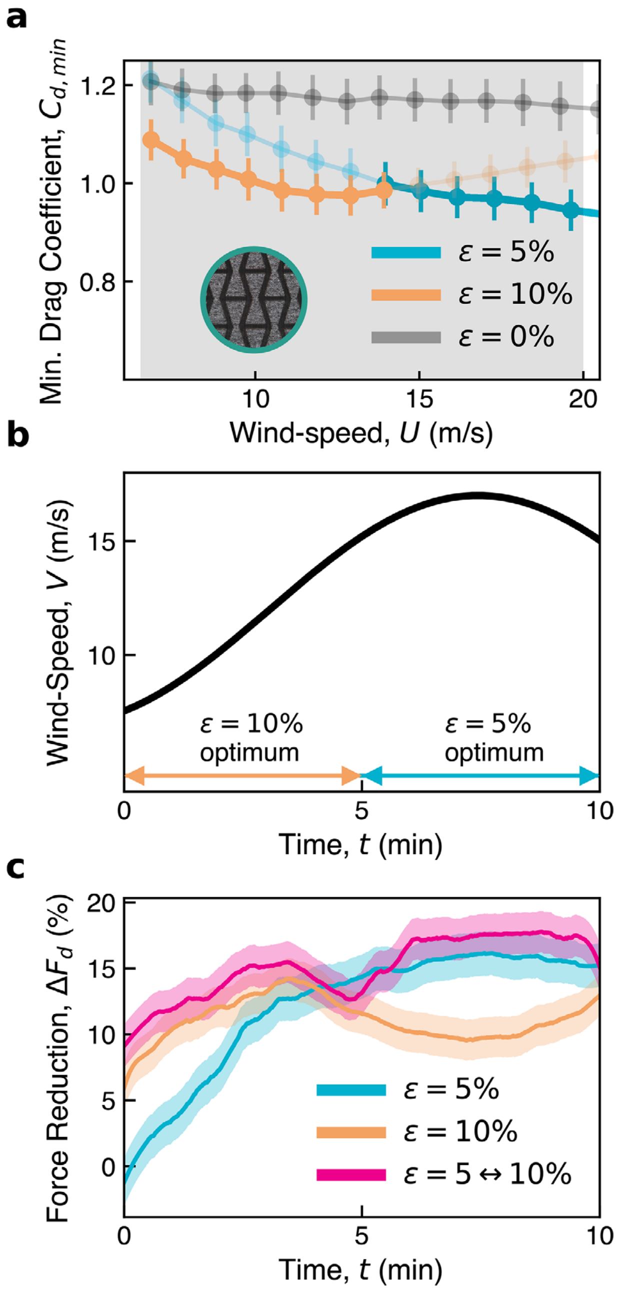

Figure 5. Active Dimpling Control. a) Drag coefficient (C_d) as a function of wind speed (U) for sample G2. For $6.5 < U < 15$ and $15 < U < 20$, C_d is minimized by selecting $\varepsilon = 10\%$ and $\varepsilon = 5\%$, respectively. Error bars indicate standard deviation for each averaged time-period. b) Selected wind speed profile. c) Temporal evolution of drag force reduction relative to the unstretched sample for three different stretching conditions, presented with smoothed experimental data (solid line) and residual standard deviation (shaded area).

the first 5 minutes and $\varepsilon = 5\%$ for the remaining 5 minutes. To validate these predictions, we conducted aerodynamic experiments using the specified wind speed profile on sample G2 under four conditions: unstretched ($\varepsilon = 0\%$), prestretched with a constant $\varepsilon = 5\%$, prestretched with a constant $\varepsilon = 10\%$, and actively switched, with $\varepsilon = 10\%$ applied for $t \in [0, 5]$ min followed by $\varepsilon = 5\%$ for $t \in [5, 10]$ min. The results are shown in Figure 5c, where we present the temporal evolution of the drag force reduction relative to the unstretched sample, calculated as:

$$\Delta F_d = 1 - \frac{F_d}{F_d(\varepsilon = 0\%)} \tag{5}$$

where F_d is the drag force measured for the prestretched sample, and $F_d(\varepsilon = 0\%)$ is the drag force with no pre-stretch. Consistent with the results in Figure 5a, maintaining a constant strain of $\varepsilon = 10\%$ achieves a drag reduction of approximately 10% during the first 5 minutes. Then, as wind speeds exceed 15 m/s, ΔF_d decreases, reflecting the adverse aerodynamic effects of larger dimples induced by 10% strain at higher wind speeds. Conversely, when a constant strain of $\varepsilon = 5\%$ is applied throughout the test, ΔF_d is initially low during the first 5 minutes. However, as wind speeds exceed 15 m/s, ΔF_d increases to approximately 15%. Crucially, active adaptation of the dimpling strain ($\varepsilon = 5 \leftrightarrow 10\%$) allows us to combine the strengths of both configurations, achieving maximum drag reduction throughout the velocity profile. As such, these results confirm that by actively controlling the applied pre-stretch, we can ensure peak aerodynamic performance across varying wind speed conditions.

3. Conclusion and Outlook

In conclusion, this study introduces a dimpling mechanism in wearable textiles, enabling programmable surface roughness and active tuning of aerodynamic profiles. Through this mechanism, we have demonstrated that auxetic patterns can support mesoscale dimples that modulate surface roughness, even when tightly fitted to a body or object. In comparison to existing methods of surface roughness control,[23–25] the dimpling mode presented here is non-intrusive and through a fitted membrane can achieve changes in surface roughness by up to 600%. FE simulations were utilized to predict dimple performance based on geometry and applied input deformation. Aerodynamic testing highlighted the dimpling mechanism's capability to vary aerodynamic properties, allowing us to modulate aerodynamic drag by up to 20%. Furthermore, we showcased the textile's capacity to actively adjust aerodynamic behavior under dynamic loading conditions, marking a significant advantage over conventional methods dependent on static roughening elements.

Looking forward, research in textile metamaterial dimpling should focus on specific high speed applications, such as cycling and down-hill skiing. Each domain presents unique challenges that require extensive testing that takes into account: equipment, athlete posture, environmental conditions, body-curvature, and actuation methods (either automated or manual) to stretch and adjust aerodynamic dimples. Additionally, future research should explore the use of Computational Fluid Dynamics (CFD) to optimize metamaterial geometries based on target drag coefficient and wind speeds. Furthermore, although the aerodynamic forces at the wind speeds used in this study were not sufficient to significantly alter, split, or collapse the dimples, we expect such effects to occur at much higher wind speeds. This fluid-structure interaction offers an intriguing direction for future studies.

Beyond wearable technology, textile dimpling opens promising avenues for surface roughness control of bodies or objects, offering exciting opportunities in fluid-dynamic optimization for aerospace, maritime, and civil engineering systems. Continued investigations will build on this foundational work to develop the next generation of applied aerodynamic metamaterials, unlocking new strategies for performance control and optimization in wearables and beyond.

4. Experimental Section

Details on the fabrication of textile metamaterials samples are provided in Section S1 (Supporting Information). The experimental setups and procedure used to characterize the mechanical, surface, and aerodynamic properties are described in Section S2 (Supporting Information). Information on the FE simulations and modeling can be found in Section S3 (Supporting Information).

Supporting Information

Supporting Information is available from the Wiley Online Library or from the author.

Acknowledgements

The authors gratefully acknowledge support form the National Science Foundation (NSF), award numbers DMR-2011754. A.E.F. acknowledges the support of UKRI Grant Number MR/X035506/1. The authors thank H. Read and K. Mahadevan for textile graphics and knowledge. The authors also thank R. Sourki for initial code efforts.

Conflict of Interest

The authors declare no conflict of interest.

Author Contributions

D.T.F., C.M.M., C.J.W., and K.B. designed the research. C.M.M. and A.E.F. developed initial fabrication process and samples. D.T.F. wrote the FEM simulation code basis, with C.M.M providing input alongside Abaqus subroutine development. D.T.F. performed fabrication of textile metamaterial samples. D.T.F designed and performed experiments, and simulations with input from C.M.M., C.J.W., and K.B. D.T.F., C.M.M., A.E.F., C.J.W., and K.B. analyzed data and wrote the paper. Finally, the study was supervised by C.J.W and K.B.

Data Availability Statement

The data that support the findings of this study are openly available in Github at https://github.com/bertoldi467collab/aerodynamic-textile-metamaterials.git, reference number 0. https://doi.org/10.5281/zenodo.14834285.

Keywords

aerodynamic, metamaterial, programmable, surface dimpling, textile, wearable

Received: March 26, 2025
Revised: May 23, 2025
Published online:

[1] F. Malizia, B. Blocken, *J. Wind. Eng. Ind. Aerodyn.* **2021**, *214*, 104673.
[2] F. Alam, H. Chowdhury, H. Moria, *Energy Procedia* **2019**, *160*, 798.
[3] T. N. Crouch, D. Burton, Z. A. LaBry, K. B. Blair, *Sports Eng.* **2017**, *20*, 81.
[4] G. Gibertini, D. Grassi, *CISM Int. Cent. Mech. Sci.* **2008**, *23*.
[5] L. Brownlie, A. Chapman, E. Banister, I. Gartshore, *Med. Sci. Sports Exercise* **1993**, *25*, S197.
[6] L. Brownlie, I. Mekjavic, I. Gartshore, B. Mutch, E. Banister, *Ann. Physiol. Anthropol.* **2008**, *6*, 133.
[7] C. Wieselsberger, *New Data on the Laws of Fluid Resistance* **1922**.
[8] Fage, J. H. Warsap, *Aeronautical Research Committee* **1929**.
[9] E. Achenbach, *J. Fluid Mech.* **1971**, *46*, 321.
[10] P. W. Bearman, J. K. Harvey, *AIAA J.* **2012**, *31*, 1753.
[11] S. Chakrabarti *Handbook of Offshore Engineering v-viii* **2005**
[12] P. W. Bearman, J. K. Harvey, *Aeronaut. Quart.* **1976**, *27*, 112.
[13] L. Oggiano, O. Troynikov, I. Konopov, A. Subic, F. Alam, *Sports Eng.* **2009**, *12*, 1.
[14] L. Oggiano, S. L. Roar, B. L. Morten, H. Brian, *Proc. Eng.* **2012**, *34*, 15.
[15] Y. Moon, J. Song, K. Kwon, O. Kwon, M. Kim, S.-H. Yoon, B. Yunghwan, A.-N. Sa, *J. Eng. Fiber. Fabr.* **2016**, *11*, 155892501601100409.
[16] H. Moria, H. Chowdhury, F. Aldawi, F. Alam, *Proc. Eng.* **2013**, *56*, 297.
[17] H. Chowdhury, F. Alam, A. Subic, *Proc. Eng.* **2010**, *2*, 2517.
[18] L. Oggiano, L. Brownlie, O. Troynikov, L. M. Bardal, C. Sæter, L. Sætran, *Proc. Eng.* **2013**, *60*, 91.
[19] G. H. Kuper, E. Sterken, *Sports Tech.* **2008**, *1*, 189.
[20] V. N. Esfahani, V. Rajavarothayam, K. Quan, R. Hanson, P. Lavoie, *J. Wind. Eng. Ind. Aerodyn.* **2024**, *253*, 105847.
[21] A. Ward-Smith, *J. Biomech.* **1984**, *17*, 339.
[22] E. McFarland, *Am. J. Phys.* **1986**, *54*, 513.
[23] M. Guttag, P. M. Reis, *Phys. Rev. Fluids* **2017**, *2*, 123903.
[24] M. Guttag, D. Yan, P. M. Reis, *Adv. Eng. Mater.* **2019**, *21*, 7.
[25] D. Terwagne, M. Brojan, P. M. Reis, *Adv. Mater.* **2014**, *26*, 6608.
[26] J. Xie, J. B. McGovern, R. Patel, W. Kim, S. Dutt, A. D. Mazzeo, *Adv. Eng. Mater.* **2015**, *17*, 951.
[27] H. Moria, H. Chowdhury, F. Alam, A. Subic, *Sports Tech.* **2012**, *4*, 171.
[28] H. Moria, F. Alam, H. Chowdhury, A. Subic, *Proc. Eng.* **2012**, *34*, 56.
[29] L. Bardal, R. Reid, *Proc. Eng.* **2012**, *34*, 44.
[30] X. Li, J. Mao, W. Chen, P. Zhou, X. Zhang, *Inter-Noise and Noise-Con Congress and Conference Proceedings* **2024**, *270*, 5724.
[31] S. Yang, K. Khare, P.-C. Lin, *Adv. Funct. Mater.* **2010**, *20*, 2550.
[32] Y. Tan, B. Hu, J. Song, Z. Chu, W. Wu, *Nano-Micro Lett.* **2020**, *12*, 101.
[33] W. Wong, S. Pellegrino, *J. Mech. Mater. Struct.* **2006**, *1*, 3.
[34] W. Wong, S. Pellegrino, *J. Mech. Mater. Struct.* **2006**, *1*, 27.
[35] T. Wang, Y. Yang, C. Fu, F. Liu, K. Wang, F. Xu, *J. Mech. Phys. Solids* **2020**, *134*, 103738.
[36] K. Bertoldi, V. Vitelli, J. Christensen, M. v. Hecke, *Nat. Rev. Mater.* **2017**, *2*, 17066.
[37] E. Barchiesi, M. Spagnuolo, L. Placidi, *Math. Mech. Solids* **2017**, *24*, 212.
[38] X. Yu, J. Zhou, H. Liang, Z. Jiang, L. Wu, *Prog. Mater. Sci.* **2018**, *94*, 114.
[39] H. M. A. Kolken, A. A. Zadpoor, *RSC Adv.* **2017**, *7*, 5111.
[40] L. J. Gibson, M. F. Ashby, Cellular Solids: Structure and Properties, 2nd ed., Cambridge Solid State Science Series, Cambridge University Press, **1997**.
[41] E. Maskell, *A theory of the blockage effects on bluff bodies and stalled wings in a closed wind tunnel* **1963**.
[42] R. W. Ogden, *Proceedings of the Royal Society of London. A. Mathematical and Physical Sciences* **1972**, *326*, 565.
[43] A. Dixit, H. S. Mali, *Mech. Compos. Mater.* **2013**, *49*, 1.
[44] D. W. Allen, D. L. Henning, *All Days* **2001**.

ADVANCED
MATERIALS

Supporting Information

for *Adv. Mater.*, DOI 10.1002/adma.202505817

Programmable Surface Dimpling of Textile Metamaterials for Aerodynamic Control

*David T. Farrell, Connor M. McCann, Antonio Elia Forte, Conor J. Walsh and Katia Bertoldi**

Supporting Information

Programmable Surface Dimpling of Textile Metamaterials for Aerodynamic Control

David T. Farrell[1], Connor M. McCann[1], Antonio Elia Forte[1,2], Conor J. Walsh[1] and Katia Bertoldi[1]

[1]John A. Paulson School of Engineering and Applied Sciences, Harvard University, Cambridge, MA, USA
[2]Department of Engineering, King's College London, London, UK

June 25, 2025

Contents

---

*Correspondence to bertoldi@seas.harvard.edu

S1 Fabrication

The textile metamaterial platform was developed to facilitate rapid prototyping and iteration of advanced textile structures. In this section, we describe our methods for textile metamaterial fabrication. Supplemental Video 1 provides additional content about the manufacturing process.

S1.1 Textile Metamaterial Fabrication

A textile metamaterial is a class of textile that combines a stiff woven with a stretchable knit. For the work described in this paper, we sourced two textiles, a nylon woven (70 denier from Seattle Fabrics) and a compliant spandex knit (custom circular knit from New Balance). The nylon woven was selected for its high stiffness and fine yarn count (70 D.), which keep the fiber scale below the laser-cut feature size; additionally the pre-applied thermal adhesive was an added benefit for ease of manufacturing. The spandex knit was chosen for its stretch, durability, and nearly isotropic mechanical response. Textile metamaterial samples are fabricated in a two step process that requires only the use of a laser cutter and a heat-press. First, we use the Versa Laser Cutter (Universal Lasers VLS6.60) to cut both textiles to the correct dimensions, for the woven material we also cut a given lattice pattern, such as hexagonal or triangular lattice. The laser cutter parameters were calibrated for textile cutting, which required reduced laser power and reduced cutting speed.

For the case of the woven structure, during the laser cutting process a unit-cell lattice is cut into the woven in a subtractive manufacturing process. Due to innate length scale of the yarn structure, there is a limitation on the width of the woven ligament. For the current study, the unit-cells were limited to a ligament width of 2.25mm. The two textiles layers are then glued via a thermally activated adhesive between the layers. In the case of our nylon woven, a thermoplastic polyurethane (TPU) coating came pre-applied to the textile without the need for additional processing. The two layers were then combined using a Geo-Knight DK20SP heat-press, set to 180 °C and a pressure of 90 psi. Samples were pressed for 25 seconds, before being rotated and pressed again. The rotation ensured even pressure distribution from the heat-press during the bonding process.

In the case of cylindrical textile metamaterial samples, a third manufacturing step was required to create cylindrical geometries. Samples were fabricated and bonded in a rectangular form that matched the height and circumferences of the testing cylinder. The thickness of the composite textile, approximately ≈ 0.65 mm, was considered to ensure that the tangential strain was zero when fitted onto the cylinder. The textile was then formed into a cylinder and sewn using a ActiveSeam flat overlock stitch on a Merrow MB4DFO 2.0 machine. This stitch is flat and stretchable along the axial direction while remaining stiff in the circumferential direction of the cylinder.

S2 Experiments

In this section, we describe the experiments that were conducted to characterize the surface changes of the planar and cylindrical samples. Then we provide details on the aerodynamic testing conducted in the wind-tunnel experiments.

S2.1 Planar samples

Planar samples were fabricated and tested both to characterize surface topology and mechanical properties.

S2.1.1 Dimple Characterization

To characterize the surface morphology of the planar samples we used an experimental setup consisting of three components (Figure S1a): laser profiler (Keyence LJ-X8200), a sample mount with stretching-rail, and a uniaxial testing machine (Instron 68TM-10), here employed simply as a high-accuracy linear actuator. The profiler sampled the surface profile through a 1-D line with approximately 3200 points evenly spaced by 25µm (x-axis). The surface information (z-axis) was captured at each sample point with a height accuracy of ±27µm. The Instron was used simply as linear actuator, translating the 1-D profile line across the sample at 12 mm/s. The laser profiler sampled the profile at a rate of 1000 Hz, providing an approximate resolution of 1-sample per 12 µm in the y-direction. The resolutions utilized here were chosen to ensure that high-fidelity scans of the textile surface were taken which captured the underlying textile yarn-structure.

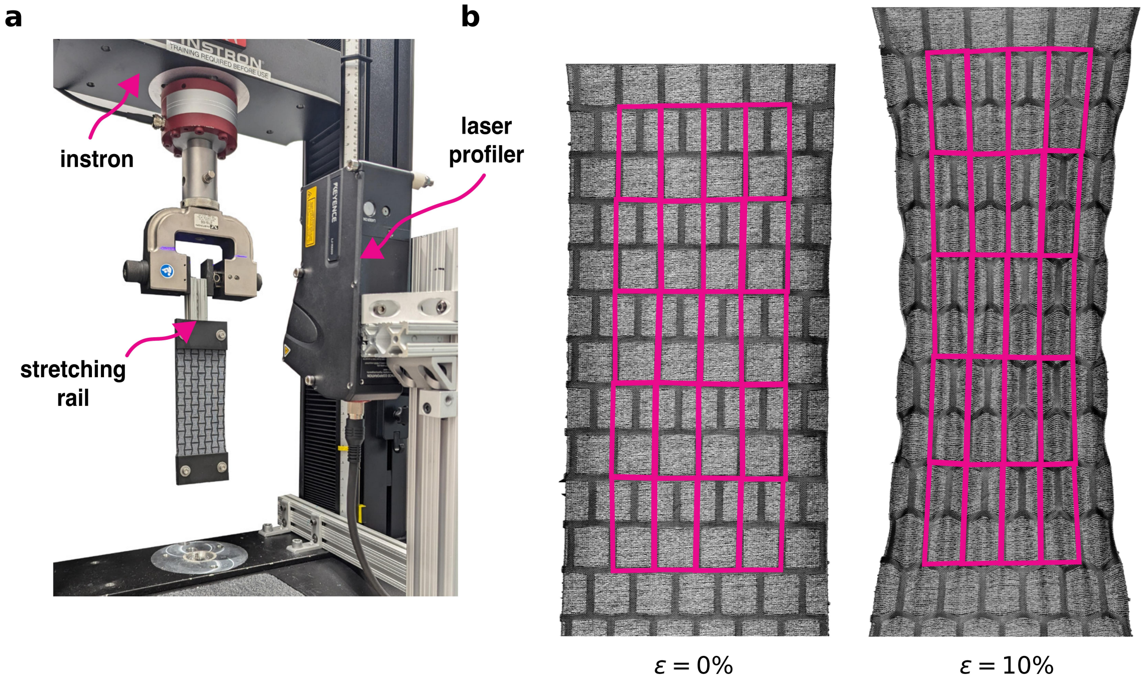

Figure S1: **Planar Scanning Experiment.** **a,** Photograph of planar scanning setup, we use an Instron 68TM-10 to linearly translate a textile sample across the 1D scan line of a laser profiler (Keyence LJ-X8200). **b,** Textile metamaterial unit cells are segmented at $\varepsilon = 0\%$ and then tracked using optical flow techniques.

For this testing, the samples were manually stretched along a linear rail in 1 mm increments with a measurement scale of ±0.5 mm. Additionally, to mitigate error due to slack in the membrane, samples were over-stretched, beyond the perscribed strain $\varepsilon > 10\%$. This over-stretching allowed adjustments and calibration of the unstretched state during post-processing. To ensure the response time of the Instron was not a factor in the velocity step, the sample was scanned over a distance greater than the sample length. Additionally, when capturing the surface profile of the sample, luminance values were also taken to help with post-processing and the graphical representation of the surface structure.

Profiler data was then post-processed in a two-step procedure. Firstly, a tilt correction was applied to the scan through a planar calibration. This ensured that any deviation in the x-y plane with respect to the profiler mounting was corrected. Secondly, the textile profile was manually segmented to allow complete unit-cells to be tracked as they undergo deformation (see Figure S1b). During segementation, the unit-cell selection criteria required whole unit cells which must be inset (at least 6 mm) from the sample boundary. These unit-cell locations were tracked between strain increments using the Lucas-Kanade optical flow method implemented in OpenCV [1]. The surface roughness $\overline{k}$ in each unit-cell was evaluated and averaged using the following function:

$$\overline{k} = \frac{1}{N}\sum_{i=1}^{N}(z_{\max,i} - z_{\min,i}), \tag{S2.1}$$

where $z_{\min,i}$ and $z_{\max,i}$ denote the minimum and maximum recorded out-of-plane displacement for the i-th unit cell and N is the number of segmented unit-cells.

S2.1.2 Mechanical Testing

Mechanical testing was conducted to fit material properties and characterize the mechanical behavior of the textile metamaterial. This testing was conducted on an Instron 68TM-10, which recorded both displacement and reaction forces.

Textile materials can be difficult to characterize, primarily due to complex nonlinear behavior and hysteresis [2, 3]. Additionally, calculating engineering stress for a textile remaining challenging due to difficulty in characterizing textile thickness. Therefore, for the remainder of this study we will discuss textile behavior in terms of line stress σ_L, which can be calculated as:

$$\sigma_L = \frac{F}{W} \tag{S2.2}$$

where F denotes the force recorded by the Instron and W is the initial width of the sample. Note that the units of line-stress are MPa×mm. In Figure S2a we show a typical set of data recorded during our tests. Each sample is cyclically stretched four times up to a maximum target strain ε. The first cycle of stretching typically exhibits an unusually high line-stress and is considered a training cycle. The next three cycles exhibit a similar mechanical response, with reduced stiffness and an offset-initial strain. During post-processing, we discard the first training cycle, and average the loading portion of the three remaining cycles while removing the strain offset. The post-processed mechanical response is shown in Figure S2b.

S2.2 Cylindrical samples

To replicate on-body constraints, it is necessary to take into account cylindrical geometries and the surface contact due to the underlying skin. To characterize textiles under these constraints, we investigated the response of textile samples wrapped around an acrylic tube.

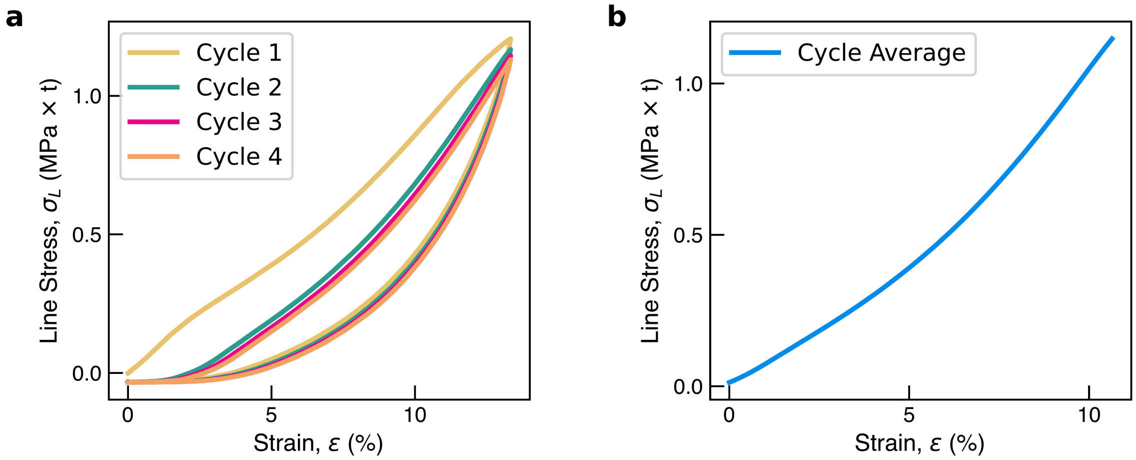

Figure S2: **Textile Mechanical Characterization.** **a,** Evolution of line stress as a function of strain during cyclic mechanical testing of a textile sample (G1). **b,** Post-processed mechanical response by averaging 2nd, 3rd, and 4th cycle and accounting for strain offset.

S2.2.1 Dimples characterization

To characterize the dimples emerging upon stretching of textile metamaterial samples wrapped around an acrylic tube, we designed an experimental setup, shown in Figure S3a. A 57.15 mm diameter acrylic cylinder was wrapped with textile metamaterial sleeves to simulate skin-tight conditions. The textile metamaterial was clamped at the bottom of the cylinder and the top of the textile was attached through hooks to a stretching platform, shown in Figure S3b. By linearly translating the platform we can stretch the textile uniformly to achieve different levels of strains.

The internal frame supporting the acrylic cylinder is mounted on rotary bearings (Figure S3a), allowing it to rotate freely around the vertical axis (z-axis). A timing belt attaches the mounting frame to an AK60 Cubemars motor with a 3:1 pulley ratio. The AK60 motor is controlled with PID velocity control, allowing the cylindrical samples to rotate at fixed angular velocities while the Keyence LJ-X8200 Laser Profiler was again used to sample the surface at a rate of 1000 samples per second. Two unavoidable sources of error are present in the experimental rig, firstly a rotational oscillation about the longitudinal axis, and a tilt error in the laser profiler placement. These errors are inherent to the experimental rig, and even after calibration can still occur on the sub-millimeter level. To correct for these errors a baseline laser profile scan was taken without an attached textile and used as a reference scan. In addition, due to the reflection of the laser beam on the acrylic surface in the absence of a textile, the cylinder was wrapped with a thin paper tube to ensure accurate readings. Following this baseline scan, the acrylic cylinder was wrapped in a textile sample, and all samples were scanned and stretched from 0% strain up to at least 10% strain. Similar to the planar case, even with careful setup the zero stretch state for the textiles ($\varepsilon = 0\%$) was difficult to obtain. Error in this setup either induced pre-strain or slack conditions in the textile. Therefore, samples were assumed slack and over-stretched, allowing for re-calibration for $\varepsilon = 0\%$ with post-processing. All scans were conducted over multiple rotations to ensure the full surface was captured, then before post-processing the data is segmented based on the stitch position to ensure one full rotation can be used for analysis.

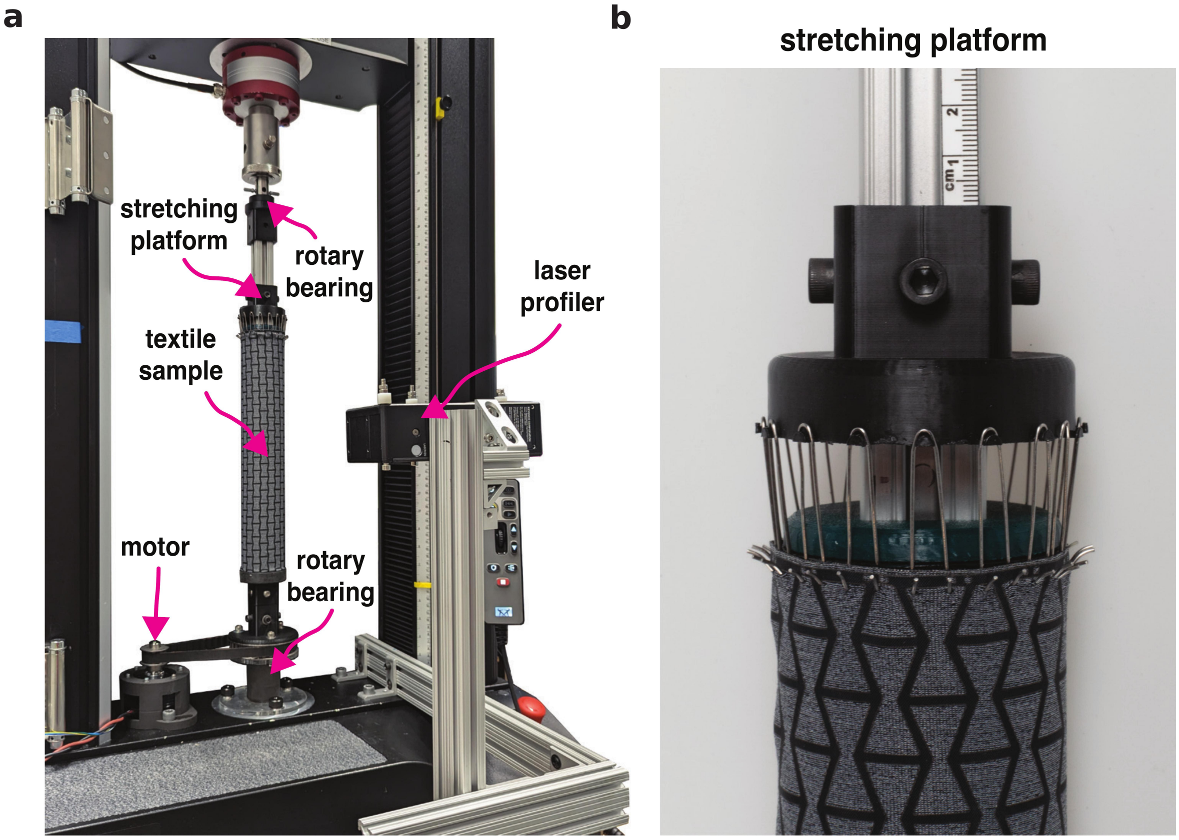

Figure S3: **Cylindrical Scanning Experiment. a,** Cylindrical samples were scanned by rotating the sample platform while being scanned via a laser profiler. **b,** Photograph of the stretching platform used to stretch textile samples.

Post-processing of the cylindrical scanning follows a similar procedure to the planar case. First, the tilt correction is applied to the cylinder to ensure a planar surface capture, this tilt correction is applied twice to increase precision, using both the baseline cylinder surface scan, and the unstretched textile case ($\varepsilon = 0\%$). The correction is applied by fitting splines to the two surfaces and then subtracting the tilt from the raw data. The result is a smooth planar scan that captures surface and dimple data accurately. The surface roughness was quantified by taking the min-max average surface roughness $\overline{k}$ of multiple unit-cells that were manually identified as shown in Figure S4. With the segmentation of these unit cells, each unit cell was tracked and the average surface roughness was calculated using Equation S2.1. Additionally, during the calculation of $\overline{k}$, in the cylindrical case a correction was implemented to ensure the lower bound of the unit-cell was not below half the initial minimum surface depth, i.e. a sample point located past the mid-line of the textile. This ensured an accurate representation from at least the textile mid-line to the top of each dimple.

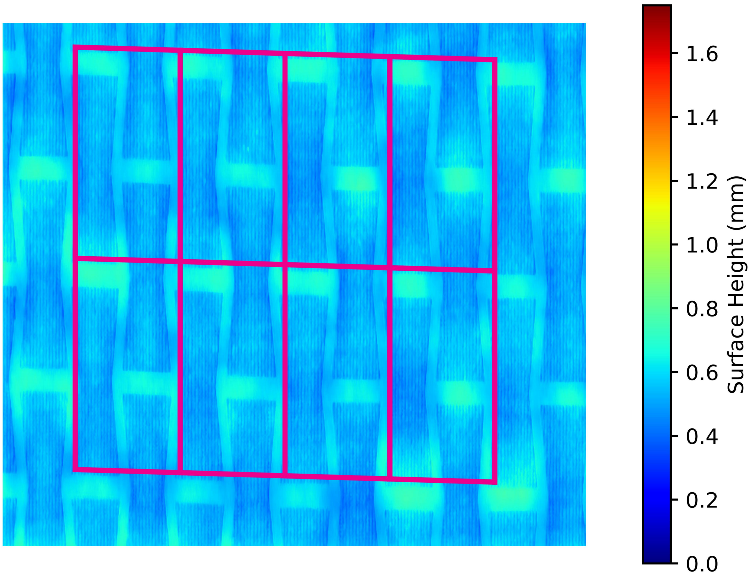

Figure S4: **Unit-Cell Segmentation.** Manual segmentation and tracking of unit-cells for surface roughness averaging of cylindrical samples.

Figure S5 presents experimental results for a re-entrant textile metamaterial with geometry G9 (as described in Figure S17). At low applied strain, large dimples form along the horizontal woven ligaments. However, as the strain increases, the textile can no longer sustain the full dimple shape and transitions into a secondary buckling mode. Eventually, at 9.7% strain, all dimples collapse into pairs of smaller dimples.

S2.2.2 Wind-Tunnel Testing

Aerodynamic testing was conducted to investigate how the aerodynamic properties of the textile metamaterial change with induced stretch. Testing was conducted on a Engineering Laboratory Design (ELD) 402A open-return wind-tunnel. The sample area for the wind-tunnel was 30.5 × 30.5 × 61.0 cm. An air velocity transducer (TSI 8455)

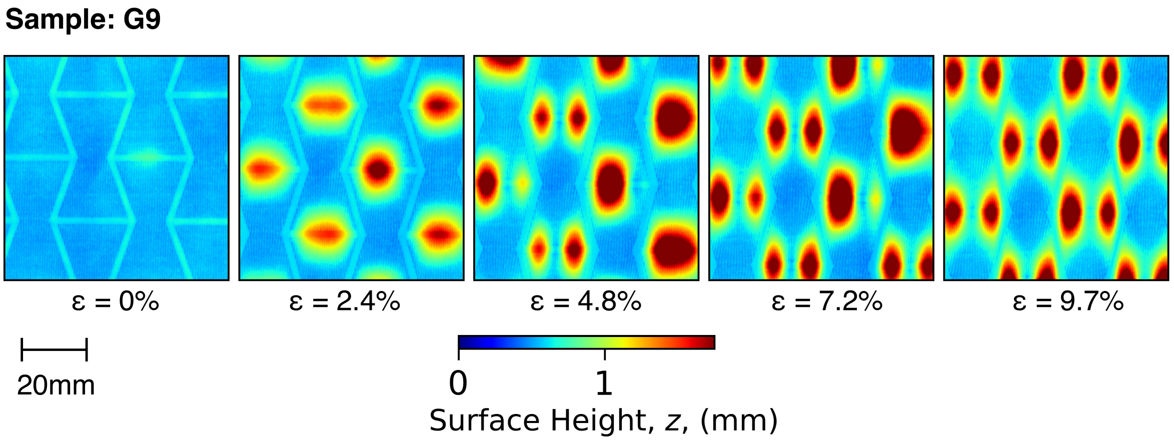

Figure S5: **Evolution of surface morphology for geometry G9.** Snapshots of the central region of re-entrant sample G9 at increasing values of applied strain, with the experimentally measured surface profile overlaid.

was placed inside the sample area to measure the incoming wind-speed (U). A textile wrapped cylinder ($D = 57.15$ mm, $L = 305$ mm) was extended through the wind-tunnel sample area, as shown in Figure S6a. The cylinder mounting frame was rigidly attached to an ATI Gamma 6-axis load-cell transducer to measure aerodynamic drag (F_d). This transducer was mechanically isolated using an external metal frame to avoid vibrational disturbances from the wind-tunnel. During operation, the wind-tunnel was controlled via a variable 10-volt DC input signal from a National Instrument DAQ, in an open-loop configuration. The type of flow in the wind tunnel was characterized via the Reynolds number. For a cylindrical sample the Reynolds number is calculated as:

$$Re = \frac{UD}{\upsilon}, \tag{S2.3}$$

where υ is the kinematic viscosity of air at room temperature (1.57×10^{-5} m^2/s).

The relatively high blockage ratio of our sample in the wind-tunnel ($\beta = DL/L^2 = 0.1875$), means a blockage correction must be considered [4, 5, 6] to account for artificially high drag coefficients. Initially an uncorrected drag coefficient, $\overline{C}_d$, was calculated as:

$$\overline{C}_d = \frac{2F_d}{\rho U^2 DL}, \tag{S2.4}$$

where; ρ denotes the density of air at atmospheric conditions (1.18 kg/m^2), F_d the aerodynamic drag force, U the wind-speed velocity, D cylinder diameter, and L the length of the cylinder in the free air-flow.

Subsequently a correction was applied through Maskell's theory [4] to calculate the corrected drag coefficient, C_d, as

$$C_d = \frac{\overline{C}_d}{(1 + \zeta\beta\overline{C}_d)} \tag{S2.5}$$

where, β is the blockage ratio and ζ is a fitting parameter. Three smooth acrylic cylinders with varying blockage ratios ($\beta = [0.1667, 0.1875, 0.2083]$ were tested. The fitting of ζ was conducted by comparing test data against well-establish values of 1.2 for smooth cylinder [7] using MATLAB function `lsqcurvefit`. The results for fitted value $\zeta = 0.343$ are shown in Figure S6b.

During textile aerodynamic characterization, the stitch of each textile cylinder was placed in the down-stream direction to avoid direct interaction with the fluid flow. Two types of wind-tunnel experiments were conducted on textile samples. Firstly the textile metamaterial dimpling was characterized through methodical testing and post-processing using Equation S2.5, and second a dynamic profile test was conducted to demonstrate the ability to active change aerodynamic properties into local optimums.

For textile aerodynamic characterization, wind-tunnel testing was conducted on each sample for 12 uniaxial stretch values, from 0% to 10% strain. When reported in the main text, these 12 strain values were down-sampled to 7 values for presentation purposes. The full 12-sample aerodynamic results have been provided in the Zenodo repository. During the testing each strain value was tested at 21 speeds between approximately 6.9 and 28.8 m/s (with an approximate increment of $\Delta U \approx 1m/s$). After each sample point, the wind-tunnel was ramped up to the subsequent point and given 25 seconds to allow the air flow to stabilize, after which 30 seconds of aerodynamic data (air velocity and force transducer data) was collected and averaged.

During the dynamic profile test, a velocity profile was generated based on approximate speeds experienced in high-speed sports such as downhill skiing and cycling. This 10-minute profile was tested on four textile states: $\varepsilon = 0\%$, $\varepsilon = 5\%$, $\varepsilon = 10\%$, and a dynamic stretching test what switched between $\varepsilon = 5\%$ and $\varepsilon = 10\%$. For the dynamic stretching test, to avoid spikes in the drag force data, the data collection was stopped for 40 seconds to dynamically change the stretch on the textile structure. All results were then compared to the $\varepsilon = 0\%$ condition and the percent change in the drag force was calculated. To post-processing the aerodynamic data, a Gaussian low-pass filter was initially applied to remove high-frequency noise. Subsequently, the data underwent smoothing using a Savitzky-Golay filter, selecting a window-size of 10,000 samples, which corresponds to 8.3% of the total data. This approach helped to maintain the integrity of the underlying aerodynamic trend while reducing noise. The residuals of this smoothing process, denoted as r_i, are computed as follows:

$$r_i = f_i - \hat{f}_i$$

where f_i is the aerodynamic drag at a specific time-point, and $\hat{f}_i$ is the force value smoothed by the Savitzky-Golay filter. The standard deviation of these residuals, representing the variability around the smoothed values, is calculated as:

$$\sigma_{\text{residual}} = \text{std}(r_i)$$

S3 Simulations

To investigate the effect of the geometry on the mechanical response of the textile metamaterial, we conducted FE simulations using the commercial software Abaqus 2021 [8].

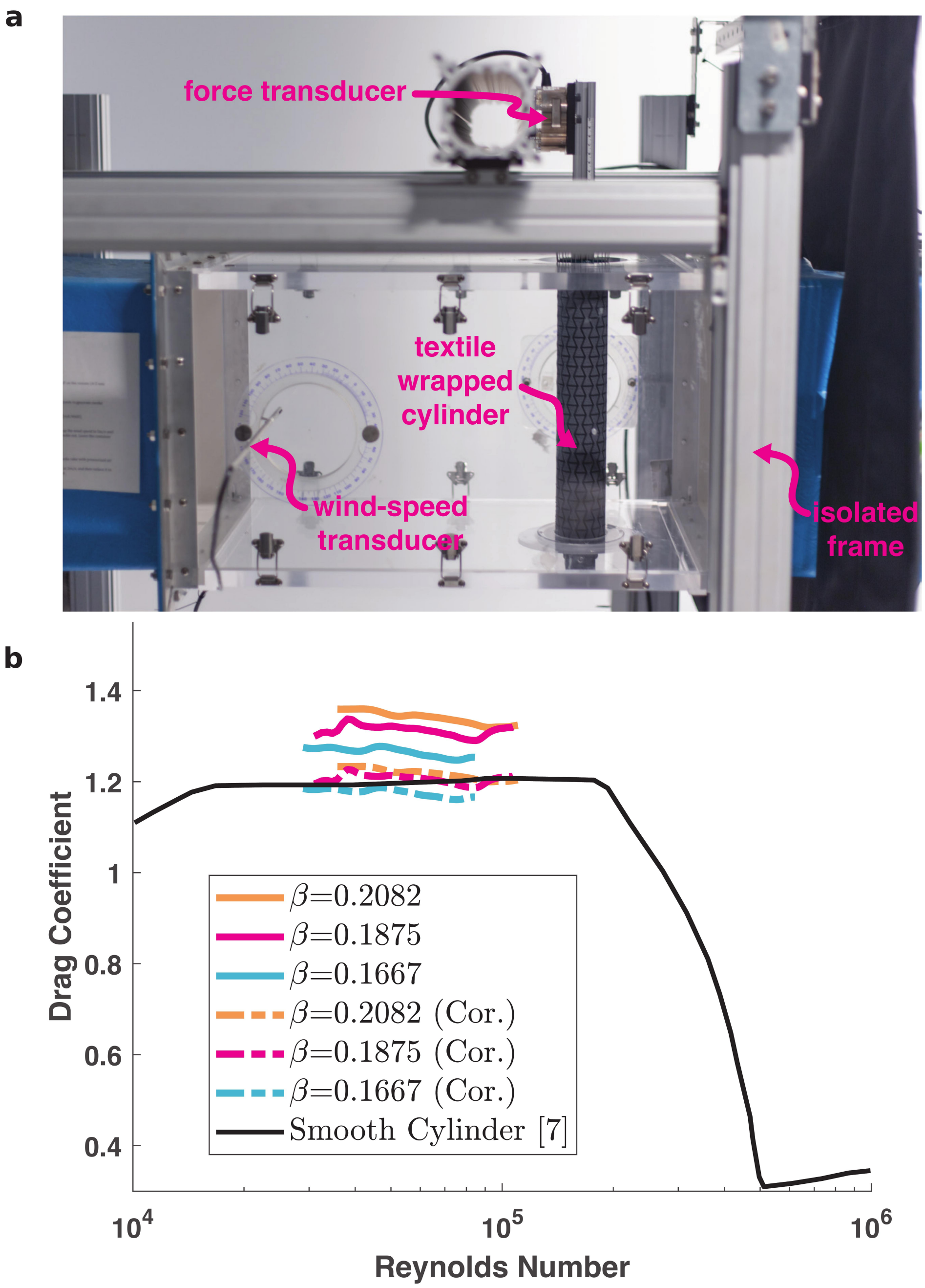

Figure S6: **Aerodynamic Experiment Overview.** **a,** Wind-tunnel sample area image, highlighting transducers to record drag force and wind-speed. **b,** Blockage factor correction fitted to varying levels of blockage factor.

For reference, all relevant codes are provided in an accompanying `Github` repository (link).

The re-entrant structure of the textile metamaterial is defined by three geometric parameters (Figure S7a): the width (w), the height (h), and the ligament angle (α).

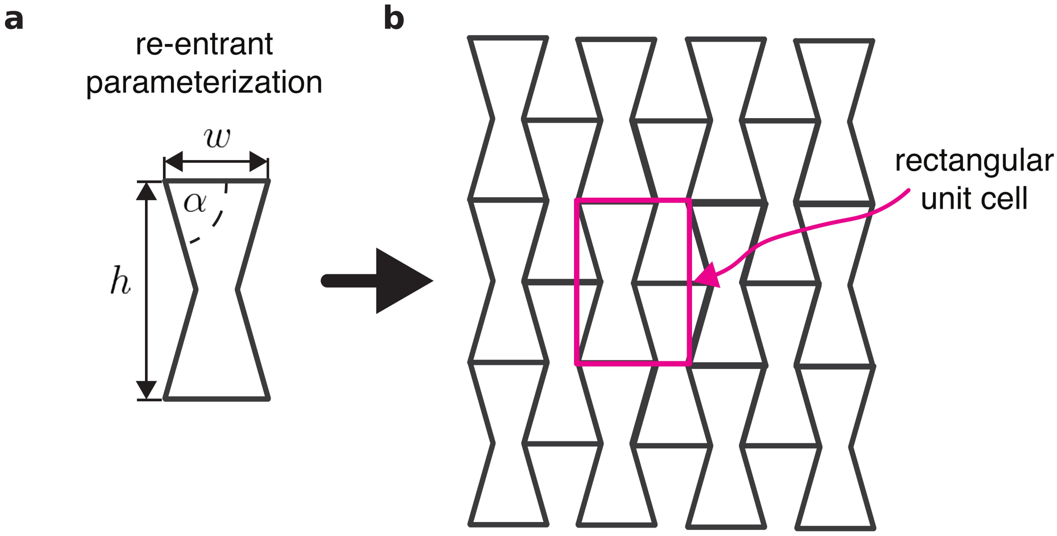

Figure S7: **Re-entrant Unit Cell. a,** Re-entrant unit-cell geometric parameters. **b,** Full re-entrant unit-cell pattern, with rectangular RVE area highlighted in magenta.

All simulations were simulated on the rectangular representative volume elements (RVEs) indicated by the magenta rectangle in Figure S7b. The RVEs were discretized using 4-node quadrilateral shell elements with hourglass control and reduced integration (Abaqus element type S4R) and 3-node triangular general purpose shell elements (Abaqus element type S3).

Each RVE comprises of both woven and knit materials. The response of the stiff woven textile was captured using an anisotropic linear lamina model, while that of the knit was captured with a hyperelastic Ogden model. Importantly, to account for asymmetry in the shell structure, the woven material was modelled with a offset shell section with the woven mid-plane rested above the knit mid-plane, ensuring accurate representation of the layered composite structure. Details on the material parameter selection are provided in Subsection S3.1.

Due to the instabilities triggered upon loading, the RVE deformation was simulated using nonlinear dynamic implicit analyses (Abaqus step type `*DYNAMIC`) with the load applied very slowly to ensure quasi-static conditions. Simulations were implemented with Rayleigh damping factors using proportional mass damping of $\alpha_R = 1.5$. All simulations were implemented using Python-based Abaqus scripting. No nodal imperfections were required for this analysis. Instead, the introduction of a structural asymmetry, due to the offset of the woven and knit sections, naturally induces a rotational moment. This asymmetry effectively breaks the geometric symmetry and results in out-of-plane deformation.

S3.1 Material Parameter Fitting

To determine the material model that captures the response of the knit and the woven, uniaxial tests were performed on samples of each material using an Instron 68TM-10 Universal Testing Machine. Due to the anisotropic nature of textile structures, samples were cut at seven different orientations: $[0°, 15°, 30°, 45°, 60°, 75°, 90°]$, with 0°corresponding to the weft direction of the textile.

Knit samples with size of 150 mm × 75 mm were subjected to uniaxial testing, as shown in Figure S8a. For the textile metamaterial designs, the woven textile is cut into narrow strips of comparable width to the underlying length-scale of the textile weave. As such, the effective homogenized material properties can depend on the width of the ligaments employed. To accommodate these scale effects of the yarn structure, strip samples were prepared and tested. Specifically, each sample contained 12 strips that were each 2.25 mm wide, as shown in Figure S8b. All metamaterial samples were subsequently prepared with the same ligament width to ensure a reliable comparison.

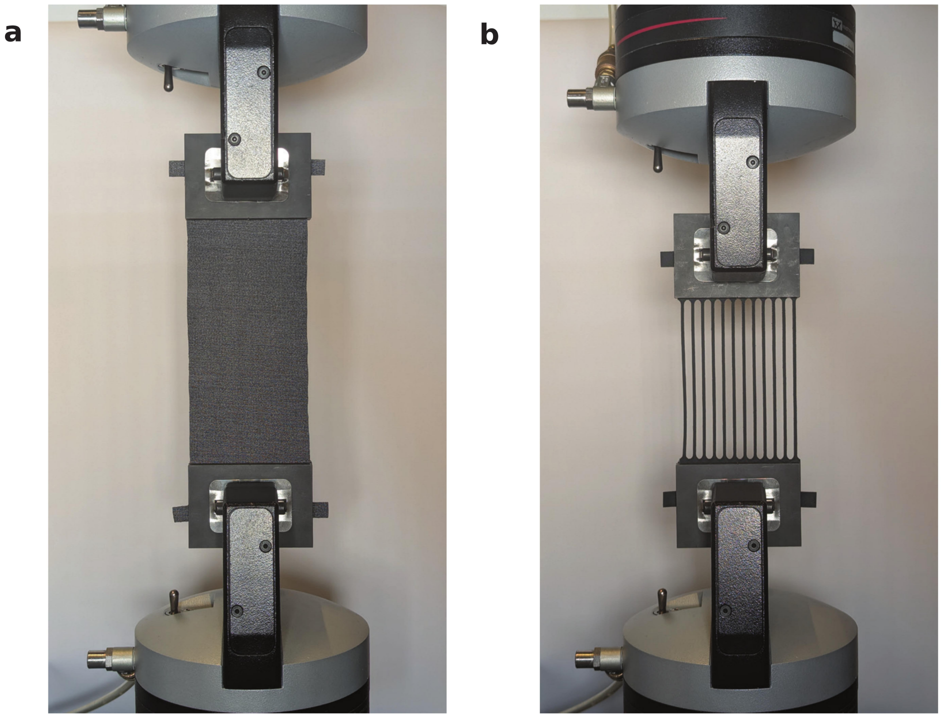

Figure S8: **Uniaxial Material Testing. a,** Uniaxial testing of knit sample (150 mm × 75 mm). **b,** Uniaxial testing of woven strip samples (12 strips of 100 mm × 2.25 mm).

Additionally, cantilever tests were conducted to estimate the bending stiffness of the woven materials. The cantilever tests consisted of four strip samples, varying both ligament length (either 35 mm or 75 mm) and textile angle (either 0° or 90°). In each experiment samples were clamped at an origin point and allowed to hang under their own weight. The end-point of the sample was manually marked and recorded based on the distance to the origin.

The knit material was extremely compliant when stretched, and exhibited near isotropic behavior when tested, as shown in Figure S10a. In comparison, the woven material, even with small strip samples, was extremely stiff and anisotropic, as shown in Figure S9a. The stiffest directions were along the warp (90°) and weft (0°) directions. This stiffness can be attributed to an alignment of woven fibers that dramatically increase stiffness along these axes. In comparison, the bias direction (45°) is the softest direction, with nearly six times lower stiffness compared to the warp direction.

Additionally, when deciding how to tune the bending stiffness for the woven textile from the cantilever tests, the decision was made to tune the shell thickness (t) based on the cantilever test results. The shell thickness of a textile is somewhat difficult to define. Added complexity arises from woven textile structure, that often exhibit high in-plane stiffness with, in contrast, relatively low bending stiffness. Although the fundamental issue in homogenizing textile based on shell theory is complex, this method of fitting shell thickness as a bending stiffness parameter allows us to get an order of magnitude closer to 'realistic' bending stiffnesses based on cantilever tests. The thickness of the knit was scaled accordingly based on the woven results. This was done by scaling based on approxiate real-life measurements of the thickness ratio of the undeformed textiles of 2.5:1.

The in-plane properties for the woven were fit using a anisotropic linear elastic lamina model. The constitutive equation for a lamina model under plane stress conditions is given in the following form:

$$\begin{bmatrix} \varepsilon_x \\ \varepsilon_y \\ \gamma_{xy} \end{bmatrix} = \begin{bmatrix} \frac{1}{E_x} & -\frac{\nu_{xy}}{E_x} & 0 \\ -\frac{\nu_{xy}}{E_x} & \frac{1}{E_y} & 0 \\ 0 & 0 & \frac{1}{G_{xy}} \end{bmatrix} \begin{bmatrix} \sigma_x \\ \sigma_y \\ \tau_{xy} \end{bmatrix} \tag{S3.1}$$

where E_x and E_y represent the Young's moduli for the two orthogonal directions, ν_{xy} is the Poisson's ratio of the material, and G_{xy} is the in-plane shear modulus. Additionally the transverse shear moduli G_{xz} and G_{yz} are incorporated as section parameters to account for shear deformation in the shell. Due to the complexity of identifying values for these material parameters (E_x, E_y, ν_{xy}, G_{xy}, G_{xz}, G_{yz}) and the shell thickness (t), a fitting optimization approach was employed. This approach utilizes the Covariance Matrix Adaption Evolutionary Strategy (CMA-ES) [9] method and is applied in conjunction with both uniaxial and cantilever simulations within the Abaqus framework.

Uniaxial simulations are conducted to determine the performance of sample material parameters (E_x, E_y, ν_{xy}, G_{xy}, G_{xz}, G_{yz}), while cantilever simulations are used to calculate the optimal shell thickness (t). The optimization process integrates these material model parameters and the shell thickness as inputs into simulation. Each iteration of CMA-ES generates a new set of material parameters and shell thicknesses. Abaqus then simulates the mechanical behavior of the samples based on these variations. The simulations outputs based on the reported strain values in the experimental data, which allows results to be directly compared without interpolation.

The error between simulation results and experimental results are quantified using the Root mean square error (RMSE), providing a measure of the error across all experiments. Specifically, the error function for the force-displacement results, denoted as RMSE_f, between experiment and simulation is given by the following function:

$$\text{RMSE}_f = \sum_{j=1}^{k} \sqrt{\frac{1}{n} \sum_{i=1}^{n} \left(\frac{F_{ij}^{\text{exp}} - F_{ij}^{\text{sim}}}{F_{nj}^{\text{exp}}} \right)^2} \tag{S3.2}$$

where, the F_{ij}^{exp} and F_{ij}^{sim} are the experimental and simulation reaction force at an i-th strain value. The RMSE is calculated and summed for each j-th testing angle

$[0°, 15°, 30°, 45°, 60°, 75°, 90°]$. The results are also normalized based on the final force $F_{exp,n}$ to make the uniaxial results and cantilever results comparable.

For the cantilever contribution to the error, we simulated the cantilever tests by applying a gravity based load to the models. As in the experiments, we simulated four models, with length β (either 35 mm or 75 mm) and textile angle α (either 0° or 90°). In the simulations we monitored a point $(x, y)_{\alpha,\beta}$ at the free end of the model and compared its coordinates to that recorded in the experiments. Specifically, in the experiments we recorded the following coordinates for the free edge of the strips are given in Table S1.

α (degrees)	β	(x, y) (mm)
0°	35	(34.925, 15.875)
0°	75	(38.1, 63.5)
90°	35	(34.925, 15.875)
90°	75	(38.1, 63.5)

Table S1: Recorded coordinates for the free end of the cantilevered strips.

Given these points, the normalized error function for the cantilever tests (RMSE$_c$) was as follows:

$$\text{RMSE}_c = \sqrt{\frac{1}{m}\sum_{i=1}^{m}\left(\left(\frac{x_{\alpha,\beta}^{\text{exp}} - x_{\alpha,\beta}^{\text{sim}}}{\text{L}_\beta}\right)^2 + \left(\frac{y_{\alpha,\beta}^{\text{exp}} - y_{\alpha,\beta}^{\text{sim}}}{\text{L}_\beta}\right)^2\right)} \tag{S3.3}$$

where $x_{\alpha,\beta}$ and $y_{\alpha,\beta}$ are the x and y component for a given textile angle α and length β combination, for the experiment and the simulation results. L_β is the strip length, i.e. 35 or 75 mm. Combined the two RMSE functions are used to calculate a total error (RMSE$_{\text{total}}$) for a given material property and thickness combination:

$$\text{RMSE}_{\text{total}} = \text{RMSE}_f + \text{RMSE}_c \tag{S3.4}$$

RMSE$_{\text{total}}$ is then minimized by CMA-ES during the optimization process. The identified optimal woven material properties from this fitting are reported in Table S2. Additionally, Figure S9 compares the numerically predicted and experimentally observed stress-strain curves alongside a polar plot of mechanical stiffness based on angular direction. From the optimization, we observe a less optimal fit for the warp (90°) direction. Due to the optimization weighting all directions equally. This is primarily due to the limitations in the Lamina model in fully capturing the extreme anisotropic behavior of a stiff woven. Essentially, to accommodate the extremely soft nature of the bias directions $(30°, 45°, 60°)$, the warp stiffness was lowered.

Table S2: Woven material properties for a linear elastic lamina material model.

$\boldsymbol{E_x}$ (MPa)	$\boldsymbol{E_y}$ (MPa)	$\boldsymbol{v_{xy}}$	$\boldsymbol{G_{xy}}$ (MPa)	$\boldsymbol{G_{xz}}$ (MPa)	$\boldsymbol{G_{yz}}$ (MPa)	$\boldsymbol{t}$ (mm)
376.4	700	0	44.3	877	600	0.067

The response of the stretchable knit was captured using a hyperelastic Ogden material model with strain energy [10]:

$$U = \sum_{i=1}^{N}\frac{2\mu_i}{\alpha_i^2}\left(\bar{\lambda}_1^{\alpha_i} + \bar{\lambda}_2^{\alpha_i} + \bar{\lambda}_3^{\alpha_i} - 3\right) + \sum_{i=1}^{N}\frac{1}{D_i}\left(J^{\text{el}} - 1\right)^{2i}, \tag{S3.5}$$

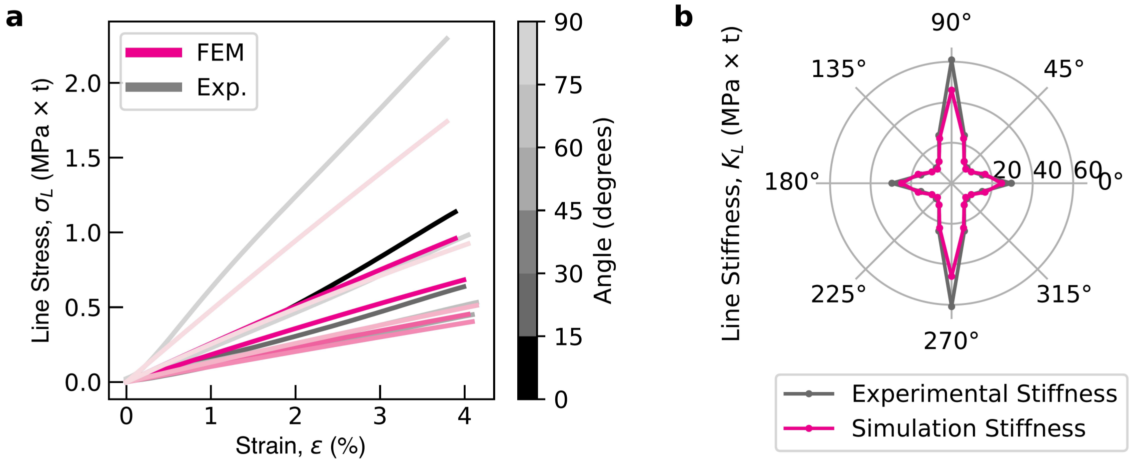

Figure S9: **Woven Mechanical Response. a,** Uniaxial mechanical response of woven textile at varying material orientations. **b,** Polar stiffness plot, based on the fitted mechanical response of experimental and simulation results.

where $\bar{\lambda}_i$ are the deviatoric principal stretches (i.e. $\bar{\lambda}_i = J^{el-\frac{1}{3}}\lambda_i$) to account for the elastic volume change given by the Jacobian $J^{el} = \det(F^{el})$; N, μ_i, and α_i are material constants, and D_i is a compressibility coefficient. The material constants N, μ_i, and α_i are determined by manually fitting the resulting stress-strain curves to the experimental ones. The material properties determined from this fitting are reported in Table S3. We assumed the knit material was incompressible ($D_1 = 0$) to reduce fitting complexity. Additionally, Figure S10 compares the experimental and numerical stress-strain curves alongside a polar plot of mechanical stiffness based on angular direction.

Table S3: Knit material properties for a hyperelastic Ogden material model.

$\boldsymbol{\mu_1}$ (MPa)	$\boldsymbol{\alpha_1}$	$\boldsymbol{D_1}$ (1/MPa)	$\boldsymbol{t}$ (mm)	$\boldsymbol{N}$
0.3	3.5	0	0.17	1

S3.2 Planar textile metamaterials

To reduce computation cost, all simulations of planar textile metamaterials were conducted using rectangular RVEs with suitable periodic boundary conditions.

S3.2.1 Periodic Boundary Conditions

The response of infinite textile metamaterials is investigated using a rectangular RVE. To subject the RVE to a macroscopic deformation gradient $\overline{\mathbf{F}}$, periodic boundary conditions are imposed on all cell boundaries [11, 12].

$$\begin{aligned}
&u_\alpha^{A_i} - u_\alpha^{B_i} = (\overline{F}_{\alpha\beta} - \delta_{\alpha\beta})(X_\beta^{A_i} - X_\beta^{B_i}),\\
&u_z^{A_i} = u_z^{B_i},\\
&\theta_\alpha^{A_i} = \theta_\alpha^{B_i},\\
&\theta_z^{A_i} = \theta_z^{B_i}, \qquad i = 1,\, 2,\, ...,\, N
\end{aligned} \tag{S3.6}$$

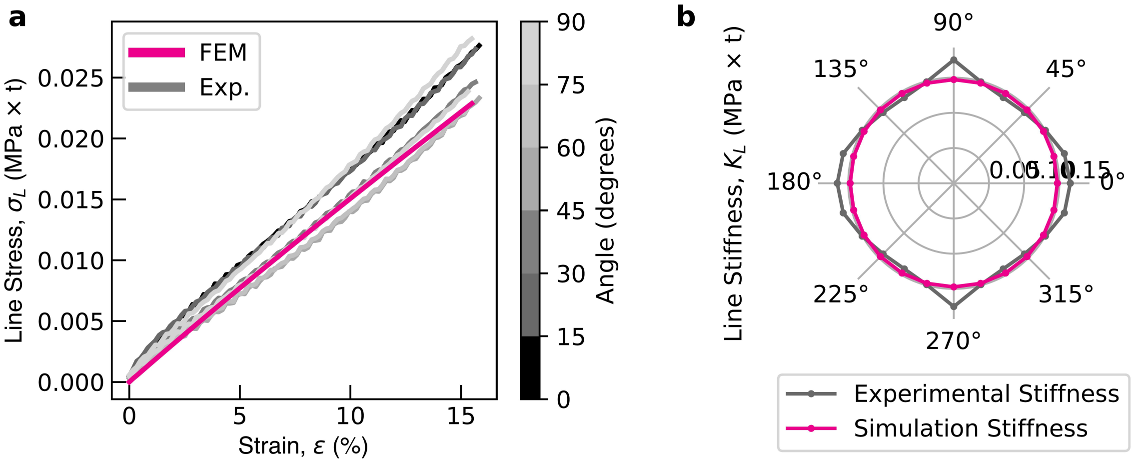

Figure S10: **Knit Mechanical Response.** **a,** Uniaxial mechanical response of knit textile at varying material orientations. **b,** Polar stiffness plot, based on the fitted mechanical response of experimental and simulation results.

where $\delta_{\alpha\beta}$ is the Kronecker delta, $u_\alpha^{A_i}$, $u_\alpha^{B_i}$, $\theta_\alpha^{A_i}$ and $\theta_\alpha^{B_i}$ ($\alpha = \{x, y\}$) are the in-plane displacements and rotational displacements of points periodically located on the boundary of the RVE. $u_z^{A_i}$, $u_z^{B_i}$, $\theta_z^{A_i}$ and $\theta_z^{B_i}$ correspond to the out-of-plane displacements and rotations. Moreover, N denotes the number of pairs of nodes periodically located on the boundary of the RVE and $X_\beta^{A_i}$ and $X_\beta^{B_i}$ are those nodes initial coordinates. An example of these boundary nodes A and B is given in Figure S11a. Note that the components of $\overline{\mathbf{F}} - \mathbf{I}$ can be conveniently prescribed within the finite element framework using a set of virtual nodes. The corresponding macroscopic first Piola-Kirchhoff stress $\overline{\mathbf{P}}$ is then obtained through virtual work considerations [11, 12]. Uniaxial tension in the y direction is applied by prescribing

$$\overline{\mathbf{F}} = F_{xx}\,\hat{\mathbf{e}}_x \otimes \hat{\mathbf{e}}_x + F_{xy}\,\hat{\mathbf{e}}_y \otimes \hat{\mathbf{e}}_y + (1+\varepsilon)\,\hat{\mathbf{e}}_y \otimes \hat{\mathbf{e}}_y + F_{yx}\,\hat{\mathbf{e}}_x \otimes \hat{\mathbf{e}}_x, \tag{S3.7}$$

where F_{xx}, F_{xy}, and F_{yx} are the deformation and shear components of the deformation matrix, which for a uniaxial test left unconstrained and determined by Abaqus by solving for $\sigma_{xx} = 0, \sigma_{xy} = 0, \sigma_{yx} = 0$. ε denotes the applied strain in the y direction (i.e. $\varepsilon_{\max} = 10\%$ in the majority of experiments). The plane stress condition $\sigma_{zz} = 0$, is handled through the shell element FEM framework, therefore when generating the equations we simply ensure the nodal displacements are periodic on the RVE boundary (e.g. $u_z^{A_i} - u_z^{B_i} = 0$).

S3.2.2 Model validation

To validate the performance of the model we compare FE simulation results against uniaxial experimental results for the textile metamaterial patterns presented in Figure 1 of the main text (i.e. square, hexagon, re-entrant, offset square, and triangular configurations).

The mechanical response of each unit-cell is shown in Figure S11b. Up to 5% strain, the FE simulations accurately capture the experimentally measured mechanical response of each unit-cell. However, the simulations encounter difficulties in accurately modeling the behavior at higher strains, particularly for the re-entrant and square lattices. Additionally, it is important to highlight the similarities in mechanical response between the re-entrant and square lattice. The mechanical response of these lattices is influenced not only by the geometry of the lattice but also the pronounced anisotropy of the woven textile, as shown in Figure S9. This influence of anisotropy can produce two structurally distinct lattices can exhibit nearly identical macroscopic stress-strain behavior in a given direction.

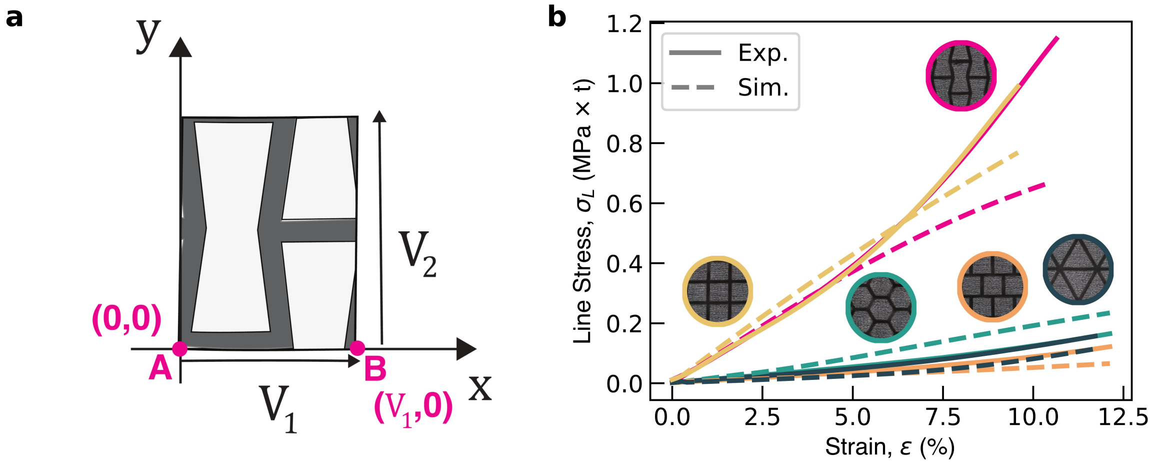

Figure S11: **Mechanical Response Textile Metamaterial.** **a,** Planar re-entrant RVE schematic. **b,** Mechanical response for common metamaterial lattices for experimental and simulation results.

Finally, it is important to note that the out-of-plane dimpling response of the textile metamaterial is also influenced by the orientation of the pattern relative to the loading direction. Rotating a given tessellation can alter both the mode and magnitude of dimple formation. To demonstrate this sensitivity, we conducted a finite element (FE) simulation on a square lattice rotated by 45° relative to the loading axis (Supplementary Figure S12). Under a uniaxial strain of $\varepsilon = 10\%$, the rotated lattice buckled into a pronounced dimpling mode, with dimples reaching a peak-to-peak height of 1.96 mm.

S3.2.3 Effective Poisson's ratio

The effective Poisson's ratio for each textile metamaterial configuration was determined by using the periodic boundary conditions discussed in Section S3.2. For these simulations a small uniaxial strain $\varepsilon = 0.01\%$ was applied. The effective Poisson's ratio was then calculated as [13]

$$\overline{\nu}_0 = -\left(\frac{F_{xx} - 1}{\varepsilon}\right). \tag{S3.8}$$

The obtained effective Poisson's ratio are shown in Figure S13b. All considered geometries exhibit a positive Poisson's ratio, with the exception of the re-entrant. The auxetic response of this membrane in response to an applied uniaxial stretch is the primary driving factor behind the dimpling response under cylindrical boundary conditions.

S3.3 Cylindrical textile metamaterials

Curved FEM models were simulated to capture the response of the textile metamaterials wrapped around a rigid cylinder. A cylindrical analytical body was generated to

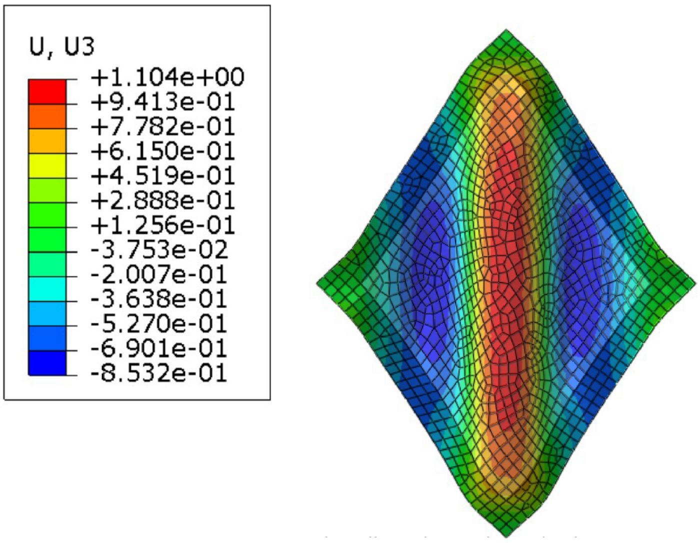

Figure S12: **45° Square Lattice** Simulated response of a square lattice planar unit-cell under periodic boundary conditions at $\varepsilon = 10\%$ strain. U3 corresponding to the out-of-plane displacement in millimeters.

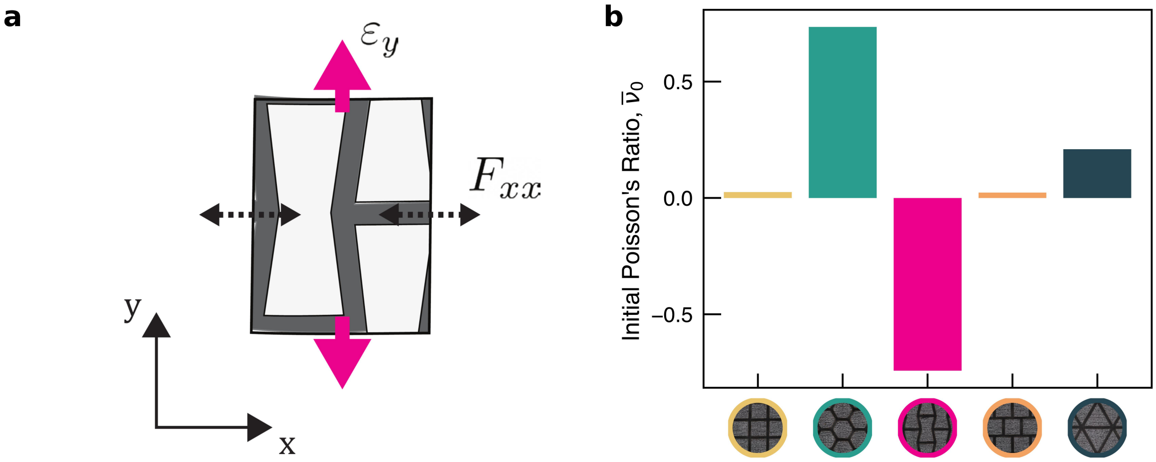

Figure S13: **Poisson Ratio Estimate. a,** Simulation protocol for RVE characterization, a small uniaxial strain of $\varepsilon = 0.01\%$ is applied in the y-direction, and the lateral contraction or expansion F_{11} is recorded. **b,** Estimated Poisson's Ratio for common metamaterial lattices based on RVE simulation.

represent the acrylic tube in the experiments. Furthermore, surface-to-surface contact was initialized between the textile metamaterial model and the rigid cylinder. To reduce computation cost, RVEs were simulated using cylindrical periodic boundary conditions applied to the unit-cell boundary.

S3.3.1 Cylindrical Mapping of RVEs

First, planar RVEs (shown in Figure S14), were mapped into cylindrical coordinates to replicate the geometry of the textile wrapped cylinder. The cylindrical diameter, including an offset of 2 × 0.25 mm to shift the shell elements to the approximate mid-point of the knit textile on both sides of the cylinder. Therefore, the thickness was defined as $D_{UC} = D + 2 \times 0.25$ mm, where D represents the diameter of the acyrlic tube (D = 57.15 mm). Notably, the cylinder circumference (πD_{UC}) does not need to be an integer multiple of the unit-cell circumferential length (V_1):

$$\frac{\pi D_{UC}}{\|\mathbf{V}_1\|} \notin \mathbb{Z} \tag{S3.9}$$

In making this assumption, when the textile lattice is wrapped around the cylinder, the unit cells will meet at an incompatible point. However, it is assumed the boundary effects arising from this incompatibility are negligible.

The Abaqus inbuilt function `wrapMesh()` was used to map the planar surface onto cylindrical coordinates, as illustrated in Figure S14. Using this function, it is assumed that the unit-cell vector magnitudes $\|V_1\|$ and $\|V_2\|$ defining the planar RVEs boundary lengths remain constant. We also assume that any bending energy incurred by wrapping the textile around the cylinder is negligible. The function takes in the diameter D_{UC} as input and applies the following relations:

$$\begin{aligned} r &= D_{UC}/2 \\ \Phi &= \frac{2 \times x}{D_{UC}}, \\ z &= y, \end{aligned} \tag{S3.10}$$

where, r is the cylinder radius, Φ represents the azimuthal angle axis, and z is the axial coordinate along its longitudinal axis, as shown in Figure S14. Through these equations, a point A with coordinates (0, 0) in the planar model will be mapped to ($D_{UC}/2$, 0, 0) in cylindrical coordinates. Following the mapping process, the node normal needs to be manually reset in the input file to ensure that they align perpendicularly to the surface of the cylinder.

S3.3.2 Periodic Boundary Conditions

Periodic boundary conditions were applied along the unit-cell boundaries to enforce continuity between matching pairs of nodes. Given that our RVE is discretized as a 2D geometry, we can assume the out-of-plane displacement is constrained to represent the shell's mid-surface, i.e. $u_r^{A_i} - u_r^{B_i} = 0$. Additionally, we can simplify this deformation further by assuming that there is rotational symmetry of our unit cell along the cylinder axis [14], i.e. $\partial[\cdot]/\partial\Phi = 0$. The simplified applied macroscopic deformation gradient in cylindrical coordinates is as follows:

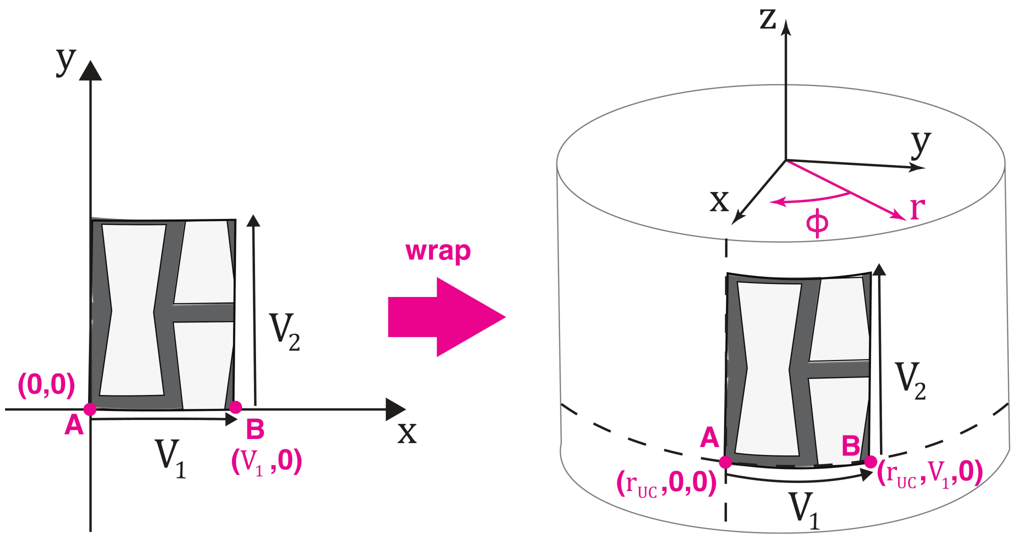

Figure S14: **Cylindrical Wrapping Function.** Re-entrant unit-cell wrapping function to transfer unit-cell mesh from Cartesian to cylindrical coordinates.

$$\overline{\mathbf{F}} = \hat{\mathbf{e}}_\Phi \otimes \hat{\mathbf{e}}_\Phi + (1+\varepsilon)\ \hat{\mathbf{e}}_z \otimes \hat{\mathbf{e}}_z \tag{S3.11}$$

where ε denotes the applied strain in the z direction. In cylindrical coordinates, the following periodic constraints were implemented along the unit-cell boundaries:

$$\begin{aligned}
&u_r^{A_i} - u_r^{B_i} = 0,\\
&u_\Phi^{A_i} - u_\Phi^{B_i} = 0,\\
&u_z^{A_i} - u_z^{B_i} = (\overline{F}_{z\beta} - \delta_{z\beta})(X_\beta^{A_i} - X_\beta^{B_i}),\\
&\theta_r^{A_i} - \theta_r^{B_i} = 0,\\
&\theta_\Phi^{A_i} - \theta_\Phi^{B_i} = 0,\\
&\theta_z^{A_i} - \theta_z^{B_i} = 0,
\end{aligned} \tag{S3.12}$$

where $\overline{F}$ is the macroscopic deformation gradient, u_α^j and θ_α^j ($\alpha = \{r, \Phi, z\}$ and $j = \{A, B\}$) are the displacement components and rotational displacements in cylindrical coordinates for the i-th pair of periodically located boundary nodes, illustrated in Figure S14.

Operationally, a multi-point constraint (MPC) subroutine was developed in Fortran, utilizing a Cartesian mapping to enforce Eqs. (S3.12). The conversion of nodal displacement from cylindrical to Cartesian is given by [14] (see Fig. S15):

$$\begin{aligned}
u_x &= u_r \cos\Phi - u_\Phi \sin\Phi,\\
u_y &= u_r \cos\Phi - u_\Phi \sin\Phi,\\
u_z &= u_z.
\end{aligned} \tag{S3.13}$$

The Cartesian displacements $(u_x^{A_i}, u_y^{A_i}, u_x^{B_i}, u_y^{B_i})$ can be represented by substituting the first two Equations (S3.12) into (S3.13), which yields:

$$\begin{aligned}
&u_x^{A_i} - \sqrt{\left(u_x^{B_i}\right)^2 + \left(u_y^{B_i}\right)^2} \cos\left(\tan^{-1}\left(\frac{u_y^{B_i}}{u_x^{B_i}}\right) - \Phi_0\right) = 0, \\
&u_y^{A_i} - \sqrt{\left(u_x^{B_i}\right)^2 + \left(u_y^{B_i}\right)^2} \sin\left(\tan^{-1}\left(\frac{u_y^{B_i}}{u_x^{B_i}}\right) - \Phi_0\right) = 0, \\
&u_z^{A_i} - u_z^{B_i} = (\overline{F}_{z\beta} - \delta_{z\beta})(X_\beta^{A_i} - X_\beta^{B_i}),
\end{aligned} \tag{S3.14}$$

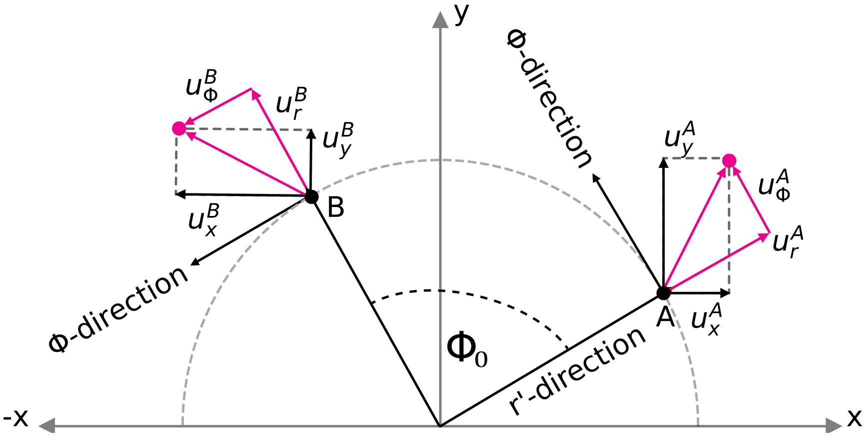

Figure S15: **Cartesian-Cylindrical Nodal Displacements.** Given two nodes, Node A and Node B, that are separated by an angle Φ_0, the displacement vectors for each node are provided in both cartesian and cylindrical coordinates.

As for the constraints in Eqs. (S3.12) that involve rotational displacements for each node (θ_r,θ_Φ,θ_z), we use Rodrigues' rotation formula [15] about the z-axis to map them from cylindrical to Cartesian coordinates. Using Rodrigues' rotation formula the last three equations in (S3.12) can be rewritten as

$$\begin{aligned}
\theta_x^{A_i} - R(\Phi_0)\theta_x^{B_i} &= 0, \\
\theta_y^{A_i} - R(\Phi_0)\theta_y^{B_i} &= 0, \\
\theta_z^{A_i} - R(\Phi_0)\theta_z^{B_i} &= 0,
\end{aligned} \tag{S3.15}$$

where $R(\Phi_0)$ denotes the axis-angle rotation using Rodrigues' rotation formula. Eqs. (S3.15) and (S3.14) were implemented via a MPC subroutine within the Abaqus framework. Given that the MPC subroutine necessitates derivatives of the above equations, the equations were symbolically generated in MATLAB (`MPC_cylindrical_PBC.m`) provided in the `Github` repository (link). The code automates the calculation of symbolic derivatives and generates a Fortran MPC scripts based on the derived expression.

S3.3.3 Validation

A series of simulations were conducted to verify proper implementation of the periodic boundary conditions.

First a homogeneous unit-cell made of a Neo-hookean material was simulated using the periodic boundary conditions of Equations (S3.14), (S3.15) and (S3.11), without the analytical rigid body or contact. An analytical respresentation of these equations were also generated for the Neohookean, where the strain energy density can be written as:

$$U = C_{10}(\bar{I}_1 - 3) + \frac{1}{D_1}(J-1)^2 \tag{S3.16}$$

where C_{10} is controls the material stiffness and shear modulus, and D_1 controls the compressability of the material. The First Piola-Kirchoff stress can be derived by taking the derivative of that U with respect to the deformation matrix F:

$$P_{ij} = \frac{\partial U}{\partial F_{ij}}, \quad i,j = \theta, z \tag{S3.17}$$

As shown in Figure S16, the numerically calculated stress-strain response closely matches the analytical model, validating the implementation of periodic boundary conditions.

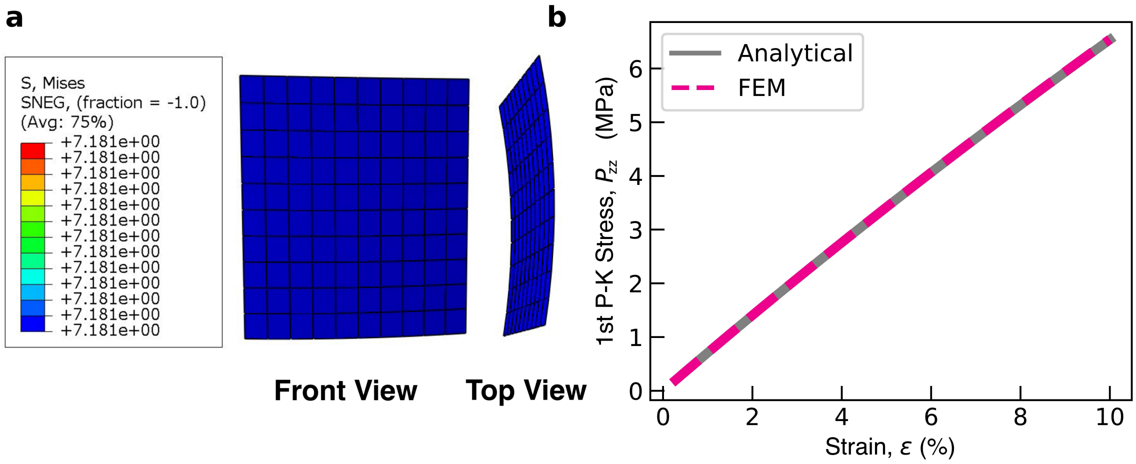

Figure S16: **Cylindrical Periodic Validation. a,** Homogeneous stress field of cylindrical unit-cell deformation under applied uniaxial load ($\varepsilon = 10\%$). **b,** Stress (1st Piola-Kirchoff, P_{22} component) vs Strain for analytical model and FEM result.

Next, we experimentally validated the response of five re-entrant structures (G5-G9) not included in Figure 4. In Figure S17b we compare experimental results with simulation outcomes for these five unit cells. Here, the tared surface roughness ($\overline{k} - \overline{k}_0$) is shown, where $\overline{k}_0$, the initial roughness of the textile due to the underlying yarn structure, is subtracted to ensure both FEM and experimental curves begin at the same roughness value.

Overall, we find good agreement between experimental results and numerical predictions, with the exception of design G9. This discrepancy can be attributed to a inaccuracy in modeling dimple collapse with high roughness-large areas re-entrant designs compared to smaller-and shallower dimples of of sample G5,G7 and G8.

S3.3.4 Dimpling of Auxetic Patterns

To confirm that auxetic behavior offers a robust mechanism for dimple formation under on-body boundary conditions, we simulated three additional auxetic textile metamateri-

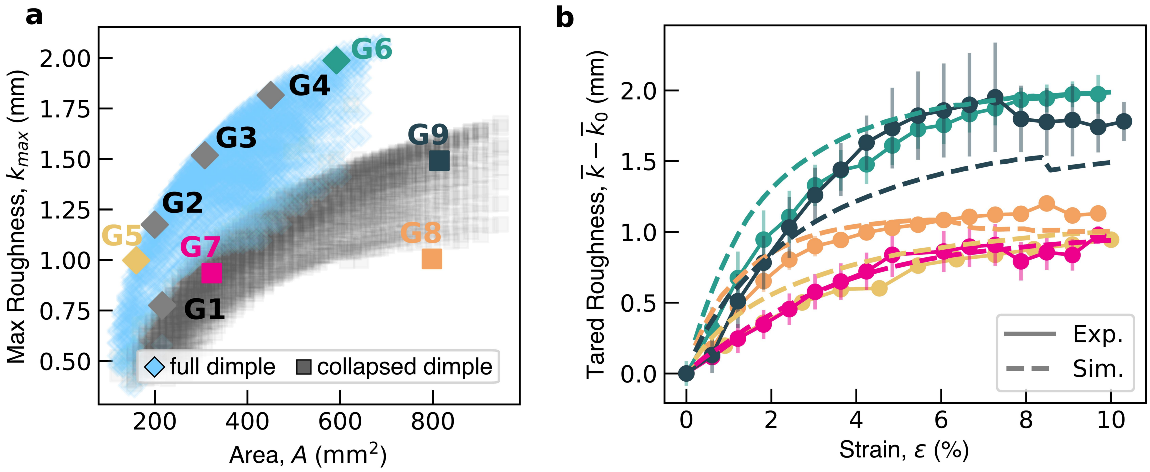

Figure S17: **Additional Dimple Model Validation.** **a,** Alongside the main paper results (G1-G4), five additional validation points were fabricated and tested in the selected design space, including two full dimples and three collapsed dimple samples. **b,** Evolution of surface roughess with respect to applie strain for five re-entrant dimpling samples (G5-G9).

als: two based on the rotating squares mechanism [16] (Fig. S18a-b) and one based on arrowhead unit cells [17] (Fig. S18c). We first simulate planar models of these three metamaterials and find that they exhibit a Poisson's ratio in the linear regime of $\bar{\nu}_0 = -0.44$, $\bar{\nu}_0 = -0.44$ and $\bar{\nu}_0 = -0.31$, respectively (calculated as described in Section S3.2.3). Notably, when wrapped around a rigid cylinder and stretched axially, dimples forms in all three sample. The two metamaterials based on the rotating squares mechanism buckles out-of-plane by up to 1 mm, forming oblong-shaped dimples (Figs. S18a-b), while the metamaterial based on the arrowhead forms 1 mm symmetric double dimples on both sides of the unit-cell (Fig. S18c). These results confirm that auxetic behavior provides a robust mechanism for enabling dimple formation under on-body boundary conditions, and exciting opportunities to target new dimple shapes with different auxetics.

S3.3.5 Effect of Material Properties

To determine the effect of material parameters on the dimple roughness, four re-entrant designs (G1-G4) from Figure 4 were selected. Each of these designs were simulated under cylindrical periodic boundary conditions while systematically varying the material properties. First, to evaluate the effect of anisotropy, we simulated the response of the designs when using an equivalent linear elastic material model. To isolate the effect of anisotropy, we first simulated each design using an equivalent linear elastic material model. The equivalent material properties for the woven material were defined as:

$$E_w^{eq} = \frac{E_x + E_y}{2} = 538\,\text{MPa}, \qquad \nu_w^{eq} = 0, \tag{S3.18}$$

and for the knit material as

$$E_k^{eq} = \frac{3\mu_1\alpha_1}{2} = 0.525\,\text{MPa}, \qquad \nu_k^{eq} = 0.5, \tag{S3.19}$$

As shown in Fig. S19a, we find that anisotropy in the woven material is not a necessary condition for dimple formation. When both the woven and knit layers are modeled as

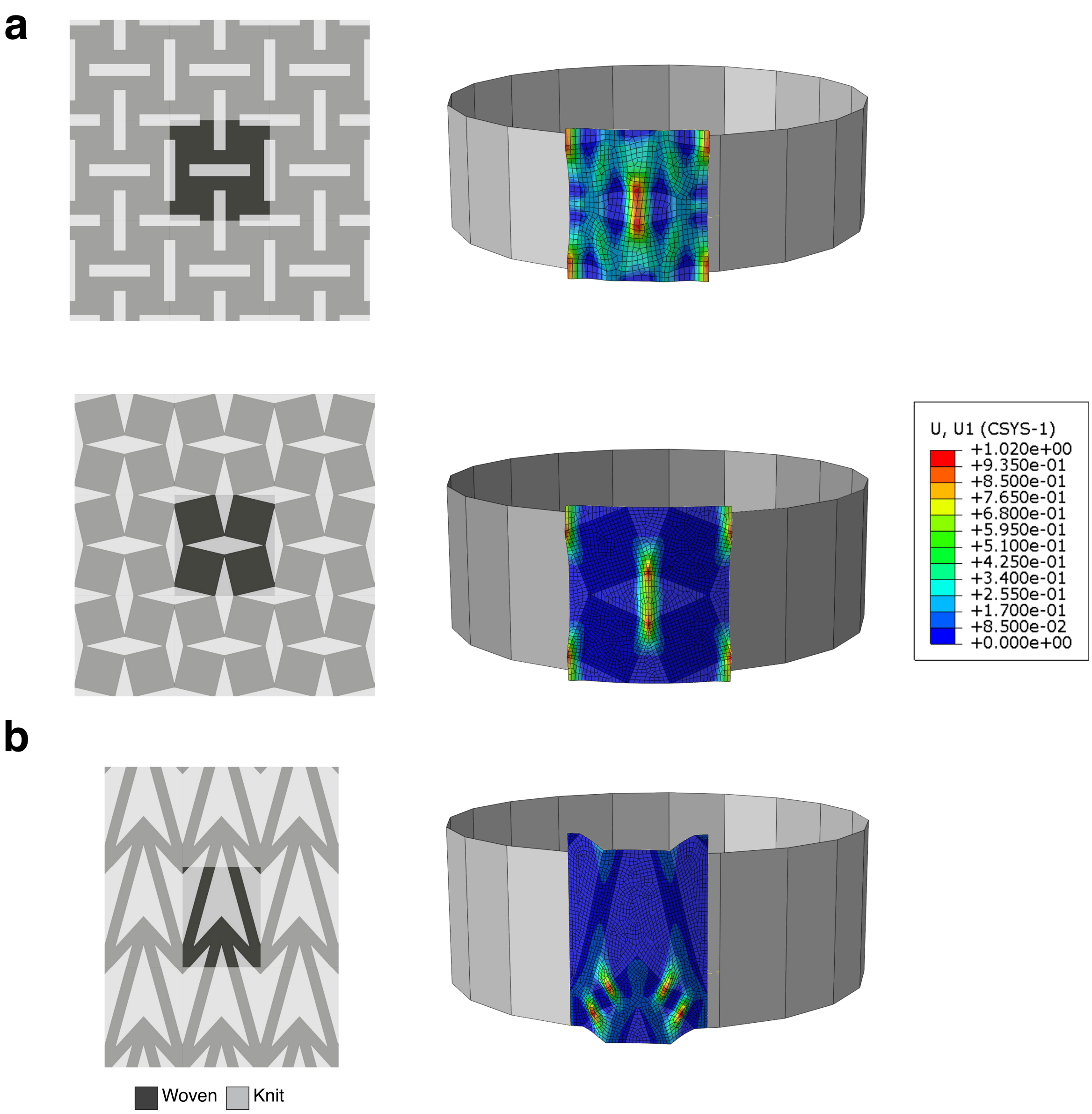

Figure S18: **Alternative Auxetic Patterns. a-b** Deformation of two cylindrical textile metamaterials based on the rotating square mechanism under uniaxial stretching ($\varepsilon = 10\%$). **c** Deformation of a cylindrical textile metamaterials based on the arrowhead unit cell under uniaxial stretching ($\varepsilon = 10\%$). Colors correspond to displacement in radial direction. All three auxetic samples exhibit dimples.

linear elastic materials, dimples still form. Similar trends are observed across all four designs, with some variations due to differences in the material models. However, the relative increase in dimple height between the different lattice designs is consistently preserved.

Next, we systematically varied the stiffness ratio between the woven and knit materials, E_w^{eq}/E_k^{eq}, while modeling both as isotropic linear elastic materials. The corresponding results are shown in Figure S19b. As the stiffness ratio decreases, the maximum surface roughness gradually reduces. In the limiting case of material with identical stiffness ($E_w^{eq}/E_k^{eq} = 1$), the textile metamaterial effectively behaves as a knit, and out-of-plane deformation is no longer observed. Additionally, for designs G3 and G4, we observe a steep drop in $k_{\max}$ occurring at approximately $E_w^{eq}/E_k^{eq} \approx 300$. This drop is primarily due to the formation of two small dimples at the ends of the horizontal ligaments under 10% strain when the stiffness ratio falls below 300, which reduces the overall dimple height.

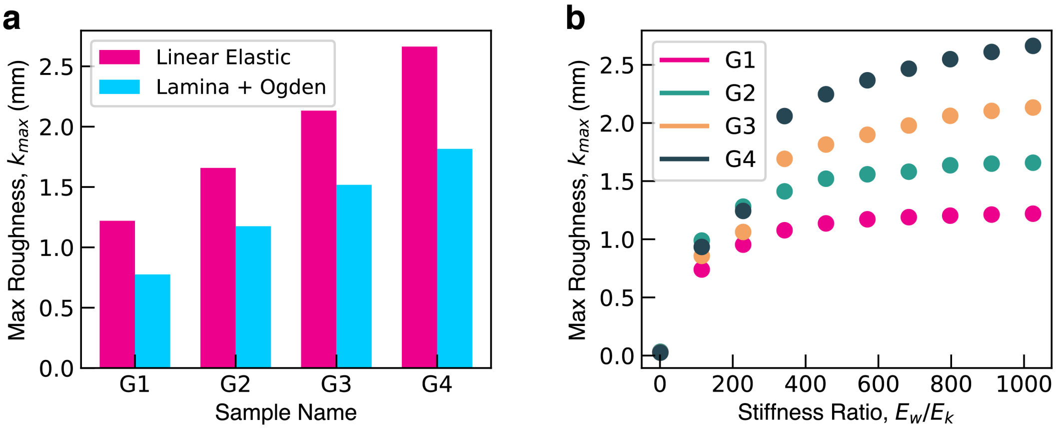

Figure S19: **FEM Material Stiffness Ratio a,** Comparison between the linear elastic estimate of material properties and the original lamina and Ogden material models, **b,** FEM cylindrical dimpling for four patterns (G1-G4) using isotropic materials with varying stiffness ratios,

S3.4 Parametric study

To systematically investigate the effect of the re-entrant unit cell geometry on dimpling, a parametric study was performed using FE unit cell simulations. Specifically, we simulated designs with $w \in [10, 22]$ mm and $h \in [12, 43]$ mm, varied in 1 mm increments (Fig. S20a). The bounds for these parameters were chosen to ensure that h and w were at least four times larger than the fixed woven ligament width of 2.25 mm, while also accommodating approximately 60 re-entrant dimples across the cylinder surface. In contrast, the ligament angle $\alpha \in [38°, 86°]$ was sampled nonlinearly within this range to account for intersections occurring at larger α, which depend on h and w. Each sample was stretched to a strain of $\varepsilon = 10\%$, and surface roughness was measured as detailed in Supplementary Section S3.4.

The results of these simulations are presented in Figure 4b of the main text and in Figure S21. Specifically, Figure S21 shows the predicted maximum dimple roughness at $\varepsilon = 10\%$ for the 3,744 simulated re-entrant unit cells, plotted as a function of width (w), height (h), and ligament angle (α).

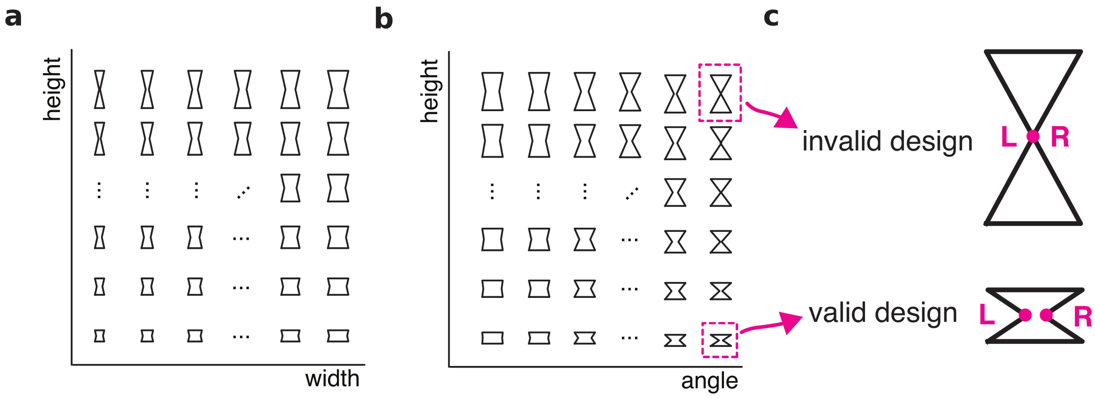

Figure S20: **Re-entrant Design Space. a,** Evolution of re-entrant designs as a function of both width and height. **b.** Evolution of re-entrant designs as a function of both angle α and height. **c.** Valid and invalid forms of re-entrant unit cells, based on the intersection of points L and R

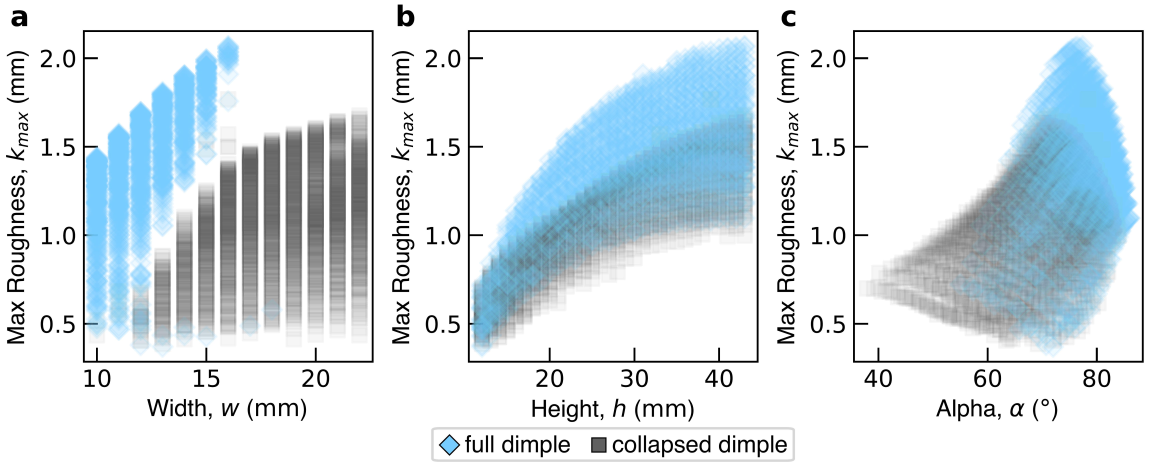

Figure S21: **FEM Geometric Parameters vs. Dimple Roughness.** Comparison of geometric parameters and the apparent impact on dimple roughness, comparing against **a,** re-entrant width, **b,** re-entrant height, **c,** and re-entrant ligament angle.

Finally, the geometric parameters for all re-entrant designs explored in this study are summarized in Table S4.

Table S4: Sample properties including maximum surface roughness ($k_{\max}$), area, width, height in mm, and α in degrees.

	$\boldsymbol{k}_{\max}$	$\boldsymbol{A}$	**Width** (w)	**Height** (h)	$\boldsymbol{\alpha}$
Sample 1 (G1)	0.78	216	12	18	78.7
Sample 2 (G2)	1.18	200	10	20	73.3
Sample 3 (G3)	1.52	308	14	22	66.0
Sample 4 (G4)	1.82	450	15	30	70.7
Sample 5 (G5)	1.00	160	10	16	67.9
Sample 6 (G6)	1.99	592	16	37	76.6
Sample 7 (G7)	0.94	323	19	17	58.4
Sample 8 (G8)	1.01	798	21	38	82.1
Sample 9 (G9)	1.49	814	22	37	70.4

S4 Supplemental Video Contents

Video 1 *Textile Metamaterial Fabrication Process*
Textile Metamaterial Fabrication. The textile metamaterial fabrication process consists of two primary manufacturing step, first the textiles are laser cut to size and the woven material is given structure through precise lattice cuts. Second, the two textiles are heat-pressed together using a heat-press and pre-applied thermal adhesive.

Video 2 *Textile Surface Dimpling*
Textile Surface Dimpling. Demonstration of dimpling phenonenon for a triangular and re-entrant (G4) textile metamaterial lattice. Both lattices are tested under planar and cylindrical boundary conditions. Under planar conditions both the triangular and re-entrant lattice exhibit dimpling behavior. In contrast, when fitted to a cylindrical structure the triangular structure dimples are suppressed and remains flat to the surface, while the re-entrant lattice exhibits surface dimpling.

References

[1] Bradski, G. The OpenCV Library. *Dr. Dobb's Journal of Software Tools* (2000).

[2] Sanchez, V., Walsh, C. J. & Wood, R. J. Textile Technology for Soft Robotic and Autonomous Garments. *Advanced Functional Materials* **31**, 2008278 (2021).

[3] Sanchez, V. *et al.* 3D Knitting for Pneumatic Soft Robotics. *Advanced Functional Materials* **33** (2023).

[4] Maskell, E. A theory of the blockage effects on bluff bodies and stalled wings in a closed wind tunnel (1963).

[5] Guttag, M. & Reis, P. M. Active aerodynamic drag reduction on morphable cylinders. *Physical Review Fluids* **2**, 123903 (2017).

[6] Guttag, M., Yan, D. & Reis, P. M. Programmable Aerodynamic Drag on Active Dimpled Cylinders. *Advanced Engineering Materials* **21** (2019).

[7] Wieselsberger, C. New Data on the Laws of Fluid Resistance (1922).

[8] Dassault Systèmes Simulia Corp. *Abaqus 2021 Documentation* (2021).

[9] Hansen, N. & Auger, A. *Principled Design of Continuous Stochastic Search: From Theory to Practice*, 145–180 (Springer Berlin Heidelberg, Berlin, Heidelberg, 2014).

[10] Ogden, R. W. Large deformation isotropic elasticity – on the correlation of theory and experiment for incompressible rubberlike solids. *Proceedings of the Royal Society of London. A. Mathematical and Physical Sciences* **326**, 565–584 (1972).

[11] Danielsson, M., Parks, D. & Boyce, M. Three-dimensional micromechanical modeling of voided polymeric materials. *Journal of the Mechanics and Physics of Solids* **50**, 351–379 (2002).

[12] Bertoldi, K. & Boyce, M. C. Wave propagation and instabilities in monolithic and periodically structured elastomeric materials undergoing large deformations. *Physical Review B* **78** (2008).

[13] Overvelde, J. T. & Bertoldi, K. Relating pore shape to the non-linear response of periodic elastomeric structures. *Journal of the Mechanics and Physics of Solids* **64**, 351–366 (2014).

[14] Fung, Y. *A first course in continuum mechanics [2nd edition]* (Prentice Hall, 1977).

[15] Cheng, H. & Gupta, K. C. An Historical Note on Finite Rotations. *Journal of Applied Mechanics* **56**, 139 (1989).

[16] Grima, J. N. & Evans, K. E. Auxetic behavior from rotating squares. *Journal of Materials Science Letters* **19**, 1563–1565 (2000).

[17] Larsen, U., Signund, O. & Bouwsta, S. Design and fabrication of compliant micromechanisms and structures with negative poisson's ratio. *Journal of Microelectromechanical Systems* **6**, 99–106 (1997).